Satellite soil moisture data assimilation impacts on modeling weather and ozone in the southeastern US - part I: an overview

Min Huang[1], James H. Crawford[2], Joshua P. DiGangi[2], Gregory R. Carmichael[3], Kevin W. Bowman[4], Sujay V. Kumar[5], and Xiwu Zhan[6]

5   [1]George Mason University, Fairfax, VA, USA
[2]NASA Langley Research Center, Hampton, VA, USA
[3]The University of Iowa, Iowa City, IA, USA
[4]Jet Propulsion Laboratory, California Institute of Technology, Pasadena, CA, USA
[5]NASA Goddard Space Flight Center, Greenbelt, MD, USA
10 [6]NOAA National Environmental Satellite, Data, and Information Service, College Park, MD, USA

Correspondence to: Min Huang (mhuang10@gmu.edu)

Abstract. This study evaluates the impact of satellite soil moisture data assimilation (SM DA) on regional weather and ozone (O_3) modeling over the southeastern US during the summer. Satellite SM data are assimilated into the Noah land surface model using an ensemble Kalman filter approach within National Aeronautics and Space Administration's Land

15 Information System framework, which is semicoupled with the Weather Research and Forecasting model with online Chemistry (WRF-Chem, standard version 3.9.1.1). The SM DA impacts on WRF-Chem performance of weather states and energy fluxes show strong spatiotemporal variability, and many factors such as dense vegetation, complex terrain, and unmodeled water use from human activities may have impacted the effectiveness of the SM DA. The changes in WRF-Chem weather fields due to the SM DA modified various model processes critical to its surface O_3 fields, such as biogenic isoprene

20 and soil nitric oxide emissions, photochemical reactions, as well as dry deposition. The SM DA impacted WRF-Chem upper tropospheric O_3 partially via altering atmospheric transport and in-situ chemical production of O_3 from lightning and other emissions. It is shown that WRF-Chem upper tropospheric O_3 response to the SM DA has comparable magnitudes with its response to the estimated US anthropogenic emission changes within two years. As reductions in US anthropogenic emissions would be beneficial for mitigating European O_3 pollution, our analysis highlights the important role of SM in

25 quantifying pollutants' transport from the US to Europe. It also emphasizes that using up-to-date anthropogenic emissions is necessary for accurately assessing the SM DA impacts on the model performance of O_3 and other pollutants over a broad region. Additionally, this work demonstrates that the SM DA impact on WRF-Chem O_3 performance at various altitudes is complicated by not only the model's emission input but also other factors such as the model representation of stratosphere-troposphere exchanges. This work will be followed by a Noah-Multiparameterization (with dynamic vegetation) based study

30 over the southeastern US, in which selected processes including photosynthesis and O_3 dry deposition will be the foci.

1 Introduction

Tropospheric ozone (O_3) is a central component of tropospheric oxidation chemistry with atmospheric lifetimes ranging from
hours within polluted boundary layer to weeks in the free troposphere (Stevenson et al., 2006; Cooper et al., 2014; Monks et
al., 2015). Ground-level O_3 is a US Environmental Protection Agency (EPA) criteria air pollutant which harms human health
and imposes threat to vegetation and sensitive ecosystems, and such impacts can be strongly linked or/and combined with
other stresses, such as heat, aridity, soil nutrients, diseases, and non-O_3 air pollutants (e.g., Harlan and Ruddell, 2011;
Avnery et al., 2011; World Health Organization, 2013; Fishman et al., 2014; Lapina et al., 2014; Cohen et al., 2017; Fleming
et al., 2018; Mills et al., 2018a, b). Across the world, various metrics have been used to assess surface O_3 impacts (Lefohn et
al., 2018). In October 2015, the US primary (to protect human health) and secondary (to protect public welfare including
vegetation and sensitive ecosystems) National Ambient Air Quality Standards for ground-level O_3, in the format of the daily
maximum 8 h-average (MDA8), were revised to 70 ppbv (US Federal Register, 2015). Understanding the connections
between weather patterns and surface O_3 as well as their combined impacts on human and ecosystem health under the
changing climate is important to developing strong-enough anthropogenic emission control to meet targeted O_3 air quality
standards (Jacob and Winner, 2009; Doherty et al., 2013; Coates et al., 2016; Lin et al., 2017).

Ozone aloft is more conducive to rapid long-range transport to influence surface air quality in downwind regions (e.g.,
Zhang et al., 2008; Hemispheric Transport of Air Pollution, HTAP, 2010, and the references therein; Huang et al., 2010,
2013, 2017a; Doherty, 2015). In the upper troposphere/lower stratosphere regions, O_3 as well as water vapor is particularly
important to climate (Solomon et al., 2010; Shindell et al., 2012; Stevenson et al., 2013; Bowman et al. 2013;
Intergovernmental Panel on Climate Change, 2013; Rap et al., 2015; Harris et al., 2015). Ozone variability in the free
troposphere can be strongly affected by stratospheric air, transport of O_3 that is produced at other places of the troposphere,
as well as in-situ chemical production from O_3 precursors including nitrogen oxides (NO_x, namely nitric oxide, NO, and
nitrogen oxide, NO_2), carbon monoxide (CO), methane, and non-methane volatile organic compounds (VOCs). Mid-latitude
cyclone is a major mechanism of venting boundary layer constituents, including O_3 and its precursors, to the mid- and upper
troposphere. It is active throughout the year and relatively weaker during the summer. Convection, often associated with
thunderstorms and lightning, is a dominant mechanism of exporting pollution in the summertime (e.g., Dickerson et al.,
1987; Hess, 2005; Brown-Steiner and Hess, 2011; Barth et al., 2012). During North American summers, anticyclones
established in the upper troposphere trap convective outflows and promote in-situ O_3 production from lightning and other
emissions (e.g., Li et al., 2005; Cooper et al., 2006, 2007, 2009).

On a wide range of spatial and temporal scales, atmospheric weather and composition interact with land surface conditions
(e.g., soil and vegetation states, topography, and land use/cover, LULC), which can be altered by various human activities
and/or natural disturbances such as urbanization, deforestation, irrigation, and natural disasters (e.g., Betts, 1996; Kelly and
Mapes, 2010; Taylor et al., 2012; Collow et al., 2014; Guillod et al., 2015; Tuttle and Salvucci, 2016; Cioni and Hohenegger,

65   2017; Fast et al., 2019; Schneider et al., 2019). As a key land variable, soil moisture (SM) influences the atmosphere via evapotranspiration. The SM-atmosphere coupling strengths are overall strong over transitional climate zones (i.e., the regions between humid and arid climates) where evapotranspiration is moderately high and constrained by SM (e.g., Koster et al., 2004, 2006; Seneviratne et al., 2010; Dirmeyer, 2011; Miralles et al., 2012; Gevaert et al., 2018). The southeastern US includes large areas of transitional climate zones, whose geographical boundaries vary temporally (e.g., Guo and Dirmeyer,

70   2013; Dirmeyer et al., 2013). Soil moisture and other land variables are currently measurable from space. It has been shown in a number of scientific and operational applications that satellite SM data assimilation (DA) impacts model skill of atmospheric weather states and energy fluxes (e.g., Mahfouf, 2010; de Rosnay et al., 2013; Santanello et al., 2016; Yin and Zhan, 2018). An effort began recently to evaluate the impacts of satellite SM DA on short-term regional-scale air quality modeling. Based on case studies in East Asia, such effects are shown to vary in space and time, and can be complicated by

75   other sources of model error, such as the uncertainty of the models' chemical inputs including emissions and chemical initial/lateral boundary conditions (Huang et al., 2018).

This study extends the work by Huang et al. (2018) to the southeastern US during intensive field campaign periods in the summer convective season. Modified from the approach used in Huang et al. (2018), we assimilate satellite SM into the Noah land surface model (LSM) within National Aeronautics and Space Administration (NASA)'s Land Information System

80   (LIS), which is semicoupled with the Weather Research and Forecasting model with online Chemistry (WRF-Chem). The term "semicoupled" here is similar to "weakly-coupled", as opposed to "fully-" or "strongly-" coupled, which indicates that the SM DA within LIS influences WRF-Chem's land initial conditions. Atmospheric states and energy fluxes from the no-DA and DA cases are compared with surface, aircraft, and satellite observations during selected field campaign periods. The WRF-Chem results are also compared with the chemical fields of the Copernicus Atmosphere Monitoring Service (CAMS),

85   which serves as the chemical initial/lateral boundary condition model of WRF-Chem. Other sources of errors in WRF-Chem simulated O_3 are identified by a WRF-Chem emission sensitivity simulation and the stratospheric O_3 tracer output from the Geophysical Fluid Dynamics Laboratory (GFDL)'s Atmospheric Model, version 4 (AM4). The modeling and SM DA approaches as well as evaluation datasets are first introduced in Section 2. Section 3 starts with an overview of the synoptic and drought conditions during the study periods (Section 3.1), followed by discussions on the model responses to satellite

90   SM DA. The SM DA impacts on O_3 export from the US and the potential impacts on European surface O_3 are included in the discussions. Results during a summer 2016 field campaign and a summer 2013 campaign are covered in Sections 3.2-3.5 and Section 3.6, respectively. Section 4 summarizes key results from its previous sections, and includes implications and suggestions on future work.

2 Methods

95   **2.1 Modeling and SM DA approaches**

This study focuses on a summer southeastern US deployment (16-28 August 2016) of the Atmospheric Carbon Transport (ACT)-America campaign (https://act-america.larc.nasa.gov). One goal of this campaign is to study atmospheric transport of trace gases. Three WRF-Chem full-chemistry simulations (i.e., base, "assim", and "NEI14" in Table 1) were conducted on a 63 vertical layer, 12 km×12 km (209×139 grids) horizontal resolution Lambert conformal grid centered at 33.5°N/87.5°W
100 (Figure 1a-c). Trace gases and aerosols were simulated simultaneously and interactively with the meteorological fields using the standard version 3.9.1.1 of WRF-Chem (Grell et al., 2005).

Version 3.6 of the widely-used, four-soil-layer Noah LSM (Chen and Dudhia, 2001) within LIS (Kumar et al., 2006) version 7.1rp8 served as the land component of the used modeling/DA system. This version of Noah is similar to Noah version 3.3 (Huang et al., 2017b, 2018), except that snow physics is based on the University of Arizona scheme (Wang et al., 2009). An
105 offline Noah simulation was performed within LIS prior to all WRF-Chem simulations for equilibrated land conditions, covering the period of 1999-2019. The "mean-state" approach (Rodell et al., 2005) was adopted to initialize Noah after cycling the model twice during this entire period. The 1/8° North American Land Data Assimilation System Phase 2 (NLDAS-2, https://ldas.gsfc.nasa.gov/nldas/v2/forcing) was used as the meteorological forcing for this spin-up. Consistent model grids and geographical inputs of the Noah LSM were used in the offline LIS and all WRF-Chem simulations.
110 Specifically, topography, time-varying green vegetation fraction, LULC type, and soil type inputs were based on the SRTM30 version 2.0, Copernicus Global Land Service, the International Geosphere-Biosphere Programme-modified Moderate Resolution Imaging Spectroradiometer (Figure 1a-c), and the State Soil Geographic (Figure S1, left, Miller and White, 1998) datasets, respectively.

Version 2 of the 9 km "enhanced" morning SM retrievals (produced using the baseline retrieval algorithm) from NASA's
115 Soil Moisture Active Passive (SMAP, Entekhabi et al., 2010) L-band polarimetric radiometer were assimilated into Noah within LIS. SMAP provides global coverage of surface (i.e., the top 5 cm of the soil column) SM within 2-3 days along its morning orbit (~6 am local time crossing) with the ground track repeating in 8 days. Compared to its predecessors that take measurements at higher frequencies, SMAP has a higher penetration depth for SM retrievals and lower attenuation in the presence of vegetation. According to SMAP Product Specification Document (https://nsidc.org/data/smap/technical-
120 references), only successful retrievals that are no smaller than the valid minimum value of 0.02 m^3 m^{-3} and of recommended quality (i.e., the retrieval quality flag has "0" values for bits 0, 1, 2) were used. Evaluation of SMAP data over North America with in-situ and LSM output suggests better data quality over flat and less forested regions (Pan et al., 2016), and previous studies have demonstrated that the SMAP DA improvements on weather variables are more distinguishable over regions with sparse vegetation (e.g., Huang et al., 2018; Yin and Zhan, 2018). Before the DA, SMAP data were re-projected
125 to the model grid and bias correction was applied via matching the means and standard deviations of the Noah LSM and SMAP data for each grid (de Rosnay et al., 2013; Huang et al., 2018; Yin and Zhan, 2018) during August of 2015-2019. Such bias correction reduced the dynamic ranges of SM from the original SMAP retrievals. The Global Modeling and

Assimilation Office (GMAO) ensemble Kalman filter approach embedded in LIS was applied, with the ensemble size of 20. Perturbation attributes of state variables (Noah SM) and meteorological forcing variables (radiation and precipitation) were

130   based on default settings of LIS derived from Kumar at al. (2009).

All WRF-Chem cases were started on 13 August 2016. Atmospheric meteorological initial/lateral boundary conditions were downscaled from the 3-hourly, 32 km North American Regional Reanalysis (NARR) which is used to derive most forcing fields of the NLDAS-2 and is generally drier and warmer than observations (e.g., Royer and Poirier, 2010; Kennedy et al., 2011). Consistent with NARR, the WRF-Chem model top was set at 100 hPa, slightly above the climatological tropopause

135   heights for the study region/month. The 0.083°×0.083° National Centers for Environmental Prediction (NCEP) daily sea surface temperature (SST) reanalysis product was used as an additional WRF forcing. Chemical initial/lateral boundary conditions for major chemical species were downscaled from the 6-hourly, 0.4°×0.4°×60-level CAMS. Surface O_3 from CAMS is positively biased over the eastern US referring to various observations, but major chemical species in the free troposphere is overall successfully reproduced (e.g., Huijnen et al., 2020; Wang et al., 2020). As WRF-Chem has only

140   tropospheric chemistry, the lack of dynamic chemical upper boundary conditions is expected to introduce biases in the modeled O_3 throughout the troposphere, and such biases depend on the distribution of model vertical layers as well as the length of the simulation. We used GFDL's AM4 and its stratospheric O_3 tracer (3-hourly, 1°×1.25°×49-level) to determine how this limitation of WRF-Chem affects its O_3 performance. The used AM4 is modified from Zhao et al. (2018), and has been applied to other O_3 studies (e.g., Zhang et al., 2019). Atmospheric meteorological and land fields were reinitialized

145   every day at 00 UTC with NARR and the previous-day no-DA or DA LIS outputs, respectively. Each day's simulation was recorded hourly at 00:00 (minute:second) through the following 30 hours, forced by temporally constant SST as the diurnal variation of the sea surface is typically smaller than land on large scales. Each day's WRF-Chem meteorological outputs served as the forcings of the no-DA and DA LIS runs, which produced land initial conditions for next day's WRF-Chem simulations. Since the second day of the simulation period, chemical initial conditions were cycled from the chemical fields

150   of the previous-day simulation. The model output >6 hours since each day's initialization was analyzed for the period of 16-28 August 2016.

In all WRF-Chem simulations, key physics options applied include: the local Mellor–Yamada–Nakanishi–Niino planetary boundary layer (PBL) scheme along with its matching surface layer scheme (Nakanishi and Niino, 2009), the Rapid Radiative Transfer Model short-/long-wave radiation schemes (Iacono et al., 2008), the Morrison double-moment

155   microphysics, which predicts the mass and number concentrations of hydrometeor species (Morrison et al., 2009), and the Grell-Freitas scale-aware cumulus scheme (Grell and Freitas, 2014), which has also been implemented in the GMAO GEOS-Forward Processing system (https://gmao.gsfc.nasa.gov/news/geos_system_news/2020/GEOS_FP_upgrade_5_25_1.php). Chemistry related configurations are: the Carbon-Bond Mechanism version Z (Zaveri and Peters, 1999) gas phase chemical

mechanism and the eight-bin sectional Model for Simulating Aerosol Interactions and Chemistry (Zaveri et al., 2008),
160 including aqueous chemistry for resolved clouds. Both aerosol direct and indirect effects were enabled in all simulations.

Daily biomass burning emissions came from the Quick Fire Emissions Dataset (Darmenov and da Silva, 2015) version 2.5r1,
and plume rise with a recent bug fix (suggested by Ravan Ahmadov, NOAA/ESRL, in August 2019) was applied. Emissions
of biogenic VOCs and soil NO were computed online (i.e., driven by the WRF meteorology) using the Model of Emissions
of Gases and Aerosols from Nature (MEGAN, Guenther et al., 2006). It has been shown that MEGAN may overpredict
165 biogenic VOC emissions and tends to underpredict soil NO emissions especially in high-temperature (i.e., >30 °C)
agricultural regions (e.g., Oikawa et al., 2015; Huang et al., 2017b, and the references therein). One possible source of
uncertainty is that the SM influences on these emissions are not well understood and represented in MEGAN. Cloud-top-
height-based lightning parameterization was applied (Wong et al., 2013). The intra-cloud to cloud-to-ground flash ratio was
based on climatology (Boccippio et al., 2001), and lightning NO was distributed using curves in Ott et al. (2010). For both
170 intra-cloud and cloud-to-ground flashes, 125 moles of NO were emitted per flash, close to the estimates in several studies for
the US (e.g., Pollack et al., 2016; Bucsela et al., 2019). Anthropogenic emissions in the base and "assim" simulations (Table
1) were based on US EPA's National Emission inventory (NEI) 2016 beta, and in a third simulation "NEI14", NEI 2014 was
used. The differences between NEI 2016 beta and earlier versions of NEIs, such as NEI 2014 and NEI 2011, are summarized
at: http://views.cira.colostate.edu/wiki/wiki/10197/inventory-collaborative-2016beta-emissions-modeling-platform,   for
175 various chemical species. Anthropogenic emissions of O_3 precursors are lower in NEI 2016 beta than in NEI 2014 (by <20%
for key species) as well as NEI 2011, in which NO_x emissions may be positively biased for 2013 (Travis et al., 2016). These
differences are qualitatively consistent with the observed trends of surface air pollutants (https://www.epa.gov/air-trends).

Chemical loss via dry deposition (i.e., dry deposition velocity multiplied by surface concentration) was calculated based on
the widely-used Wesely scheme (Wesely, 1989). This scheme defines dry deposition velocity as the reciprocal of the sum of
180 aerodynamic resistance, quasi-laminar resistance, and surface resistance. Over land, its major component surface resistance
is classified into stomatal and mesophyll resistance, cuticular resistance, in-canopy resistance, and ground resistance. Surface
resistance is usually strongly affected by its stomatal resistance component which in the Wesely scheme is expressed as
seasonal- and LULC-dependent constants (subject to large uncertainty) being adjusted by surface temperature and radiation.
This contrasts with some other approaches which also account for the influences of SM, vapor pressure deficit and
185 vegetation density, or couple stomatal resistance with photosynthesis. For calculating the nonstomatal surface resistance
components, prescribed seasonal- and LULC-dependent constants are used in the Wesely scheme, adjusted by environmental
variables such as wetness and radiation, whereas in other existing schemes, impacts of friction velocity and vegetation
density are also considered (e.g., Charusombat et al., 2010; Park et al., 2014; Val Martin et al., 2014; Wu et al., 2018; Mills
et al., 2018b; Anav et al., 2018; Wong et al., 2019; Clifton et al., 2020, and the references therein). Aerodynamic resistance
190 and quasi-laminar resistance are both sensitive to surface properties such as surface roughness.

This paper also briefly discusses in Section 3.6 some results from two WRF-Chem simulations (i.e., "SEACf" and "SEACa" in Table 1) during the 2013 Studies of Emissions and Atmospheric Composition, Clouds and Climate Coupling by Regional Surveys (SEAC[4]RS, Toon et al., 2016, https://espo.nasa.gov/home/seac4rs/content/SEAC4RS) campaign. SEAC[4]RS studies the attribution and quantification of pollutants and their distributions as a result of deep convection. These simulations were
195   conducted on a 27 vertical layer, 25 km×25 km (99×67 grids) horizontal resolution Lambert conformal grid also centered at 33.5°N/87.5°W. Their LSM and inputs, WRF physics and chemistry configurations were the same as those used in the 12 km cases described above. In "SEACa", we assimilated successfully-retrieved, daily SM from version 04.5 of the European Space Agency Climate Change Initiative project (ESA CCI) SM product (Gruber et al., 2019), developed on a 0.25°×0.25° horizontal resolution grid based on measurements from passive satellite sensors. The assimilated CCI SM data were re-
200   projected to the model grid and bias-corrected based on the climatology of Noah and CCI SM during August of 1999-2018. These simulations were evaluated with SEAC[4]RS aircraft chemical observations, which were richer than those collected during ACT-America in terms of the diversity of measured reactive chemical compounds (Section 2.2.1). Such comparisons help evaluate the emissions of O_3 precursors from various (e.g., NEI 2014 anthropogenic, lightning, and biogenic) sources as well as how the model representation of land-atmosphere interactions affects such emission assessments.

205   The model horizontal resolutions of 12 km and 25 km were set to be close to the assimilated satellite SM products to minimize the horizontal representation errors. At these resolutions, land surface heterogeneity and fine-scale processes (e.g., cloud formation and turbulent mixing) may not be realistically represented. Cloud-top-height-based lightning emissions and SM-precipitation feedbacks can be highly dependent on convective parameterizations (e.g., Hohenegger et al., 2009; Wong et al., 2013; Taylor et al., 2013). Addressing shortcomings of convective parameterizations in simulations at these scales is
210   still in strong need. Performing convection-permitting simulations with assimilation of downscaled microwave SM or/and high-resolution thermal infrared based SM (e.g., 2-8 km from the Geostationary Operational Environmental Satellite) for cloudless conditions should also be experimented in the future.

2.2 Evaluation datasets

2.2.1 Aircraft in-situ measurements during ACT-America and SEAC[4]RS

215   During the 2016 ACT-America deployment, the NASA B-200 aircraft took meteorological and trace gas measurements in the southeastern US from the surface to ~300 hPa on nine days. Different line colors in Figure 1d denote individual flight paths during this period. These flights were conducted under different weather conditions during the daytime (i.e., within 14-23 UTC, local time+6), with durations of 4-9 hours (https://www-air.larc.nasa.gov/missions/ACT-America/reports.2019/index.html). Fights on 16, 20, 21 of August 2016 sampled the air under stormy weather conditions,
220   whereas the other flights were conducted under fair weather conditions. We used meteorological as well as collocated O_3 and CO measurements collected on the B-200 to evaluate our WRF-Chem simulations. The O_3 mixing ratio measurements using the differential ultraviolet absorption has a 5 ppbv uncertainty (Bertschi and Jaffe, 2005), and CO mixing ratio was measured

with an uncertainty of 10 ppbv, using a Picarro analyzer which is based on wavelength-scanned cavity ring down spectroscopy (Karion et al., 2013). We used the weather and trace gas observations averaged in 1-minute intervals (released

225 in September 2018) for model evaluation, as they represent atmospheric conditions on comparable spatial scales to the model. Ozone and CO measurements with $O_3/CO > 1.25$ mole mole^{-1} (Travis et al., 2016) are assumed to be influenced by fresh stratospheric intrusions and were excluded in our analysis. This approach, however, was rather arbitrary and may not have excluded air that had an aged stratospheric origin.

230 Aircraft (NASA DC-8) in-situ measurements of CO, NO_2 and formaldehyde (HCHO) from the surface to ~200 hPa during six SEAC^{4}RS daytime (i.e., within 13-23 UTC, local time+6), 8-10-hour science flights in August 2013 were compared with our WRF-Chem simulations. The CO mixing ratio was measured using the tunable diode laser spectroscopy technique, with an uncertainty of 5% or 5 ppbv. The NO_2 measurements were made by two teams, based on thermal dissociation laser induced fluorescence and chemiluminescence methods, with the uncertainty of ±5% and (0.030 ppbv+7%), respectively.

235 Two other teams took the HCHO measurements, using a compact atmospheric multispecies spectrometer and the laser-induced fluorescence technique, with the uncertainty of ±4% and (0.010 ppbv±10%), respectively. Aircraft data averaged in 1-minute intervals (released in November 2018) were used, with the biomass burning affected samples (acetonitrile >0.2 ppbv) and CO from fresh-stratospheric-intrusion-affected air ($O_3/CO > 1.25$ mole mole^{-1}) excluded.

2.2.2 Ground-based measurements

240 WRF-Chem results were evaluated by various surface meteorological and chemical observations. These include: 1) surface air temperature (T2), relative humidity (RH, derived from the original dew point and air temperature data), and wind speed (WS) from the NCEP Global Surface Observational Weather Data (doi: 10.5065/4F4P-E398); 2) half-hourly or hourly latent and sensible heat fluxes measured using the eddy covariance method at eight sites within the FLUXNET network. Latent and sensible heat fluxes from this network exhibited mean errors of -5.2% and -1.7%, respectively (Schmidt et al., 2012). We

245 only analyzed the modeled energy fluxes at the sites where the model-based LULC classifications are realistic. A 0.5°×0.5°, daily FLUXCOM product was also utilized, which merges FLUXNET data with machine learning approaches, remote sensing and meteorological data. Over North America, it is estimated that latent and sensible heat fluxes from this FLUXCOM product are associated with ~12% and ~13% of uncertainty, respectively (Jung et al., 2019); and 3) hourly O_3 at the US EPA Air Quality System (AQS, mostly in urban/suburban regions) and the Clean Air Status and Trends Network

250 (CASTNET, mostly in nonurban areas) sites. Hourly AQS and CASTNET O_3 are US sources of the Tropospheric Ozone Assessment Report database, the world's largest collection of surface O_3 data supporting analysis on O_3 distributions, temporal changes and impacts. Measurements of NO_2 and HCHO are also available at some of the AQS sites. It is highly possible that these measurements are biased due to the interferences of other chemical species and therefore they were not used in this work.

2.2.3 Precipitation products

The WRF-Chem precipitation fields were also qualitatively compared with two precipitation data products: 1) the 4 km, hourly NCEP Stage IV Quantitative Precipitation Estimates (Lin and Mitchell, 2005), which is a widely-used, national radar and rain gauge based analysis product mosaicked from 12 River Forecast Centers over the contiguous US, and its quality partially depends on the manual quality control done at the River Forecast Centers; and 2) the 0.1°×0.1°, half-hourly calibrated rainfall estimates from version 6B of the Integrated Multi-satellitE Retrievals for the Global Precipitation Measurement (GPM) constellation final run product (Huffman et al., 2019). Compared with single-platform based precipitation products, multisensor based precipitation datasets have reduced limitations and therefore have become popular in scientific applications. Nevertheless, these datasets may be associated with region-, season-, and rainfall-rate dependent uncertainties (e.g., Tan et al., 2016; Nelson et al., 2016, and the references therein).

3 Results and discussions

3.1 Synoptic and drought conditions during the study periods

In August 2016, several states in the southern US experienced moderately-to-extremely moist conditions according to major drought indexes such as the Palmer Hydrological Drought Index (Figure S2, left). These were largely due to the influences of passing cold fronts and tropical systems from the Gulf of Mexico (https://www.ncdc.noaa.gov/sotc/synoptic/201608). Temperatures were consequently lower than normal in these regions. Contrastingly, controlled by the Bermuda High, more frequent air stagnation, warmer-, and drier-than-normal conditions affected multiple Atlantic states. Opposite hydrological anomalies were recorded during August 2016 and August 2013 for the southern Great Plain and Atlantic regions (Figure S2, left).

The anomalies in synoptic patterns and drought conditions in August of 2016 and 2013, as well as the day-to-day weather changes, can be closely linked to regional O_3 variability in the southeastern US. Based on the pressure gradients along the western edges of the Bermuda High (Zhu and Liang, 2012; Shen et al., 2015), the influences of the Bermuda High on southeastern US surface O_3 enhancements may be stronger in August 2016 than in August 2013 (Figure S2, middle). Lightning intensities and emissions respond to climate change (Romps et al., 2014; Murray, 2016; Finney et al., 2018), therefore affecting the probability of fires ignited by lightning. Based on satellite detections which are subject to cloud contamination, fire activities associated with emissions of heat and O_3 related pollutants were stronger in drier regions in the southern US in August of 2016 and 2013. The variable synoptic and drought conditions also controlled biogenic VOC and soil NO emissions as well as O_3-related chemical reaction and deposition rates, and the resulting impacts on O_3 depended on the changing anthropogenic NO_x emissions (Hudman et al., 2010; Hogrefe et al., 2011; Coates et al., 2016; Lin et al., 2017). In the upper troposphere, troughs bumping into the anticyclone above the southeastern US in August 2016 helped shape the

285 pollution outflows differently than in August 2013 when the North American monsoon anticyclone was built over the southwestern US and the central-eastern US was controlled by a strong cool trough (Figure S2, right).

Studies have shown that the variations in land-atmosphere coupling strength are connected with SM interannual variability and the local spatiotemporal evolution of hydrologic regime (e.g., Guo and Dirmeyer, 2013; Tuttle and Salvucci, 2016). Therefore, over the southern Great Plain and Atlantic regions, SM-atmosphere coupling strengths in August 2016 and
290 August 2013 may have diverged from the climatology in opposite directions. For example, in August 2016, the overall potential impacts of SM on surface water/energy fluxes and atmospheric states may be higher than normal over the Atlantic regions whereas below the average in the southern Great Plain. In August 2013, the land-atmosphere coupling may be stronger than normal and abnormally weak over the southern Great Plain and the Atlantic regions, respectively.

3.2 SMAP DA impacts on weather states and surface energy fluxes

295 The weather states and energy fluxes during 16-28 August 2016 from the WRF-Chem base simulation are illustrated in Figure 2 (for SM and T2), Figure 3 (for RH, WS, and PBL height, PBLH), Figure 4 (for precipitation), Figures 5 and S2 (for energy fluxes and their partitioning), together with the SMAP DA impacts on these variables.

The highest daytime (13-24 UTC, local times+5 or +6) average T2 were observed in several states in the Atlantic region that were undergoing drought conditions (Figure S2, left; Figure 2c), The daily T2 maxima occurred during noon-early afternoon
300 in most places, consistent with the findings from Huang et al. (2016). The Lower Mississippi River regions were influenced by high humidity (Figure 3c). Under the influence of the BH, surface winds were overall mild to the east of Texas. Strongest rainfall affected Texas, Arkansas, Kentucky, Tennessee, and near the border of Kansas and Missouri (Figure 4a-b), which belonged to the wetter-than-normal regions according to August 2016 drought indexes. Rainfall in most areas peaked in the late afternoon or evening after the times of peak T2 (Figure 4e-f). The observed diurnal cycles of rainfall and T2 indicate
305 that, for the study area/period, convection was mainly due to the thermodynamic response to surface temperature. However, land-sea interactions, fronts, topography, as well as aerosol loadings may also have come into play.

The dry and wet anomalies in the southeastern US based on the modeled SM (Figure 2a) are shown consistent with weekly (not shown in figures) and monthly drought indexes (e.g., Figure S2, left). The modeled SM values in various soil layers are near the model-based soil wilting points and field capacities (Figure S1, middle and right) over drought-influenced and wet
310 regions, respectively. The WRF-Chem base simulation overall captured the observed patterns of T2, RH, and WS across the domain, with its daytime PBLH spatially correlated with the T2 patterns (Figures 2b and 3a;e;i). Referring to the Stage IV and GPM rainfall data, the WRF-Chem base case also overall fairly well reproduced the diurnal cycles of rainfall during the study period, but the rainfall "hotspots" simulated by the model appear west to those in the Stage IV and GPM products (Figure 4c). Dirmeyer et al. (2012) found that models' rainfall performance more strongly depended on the distinctive

315 treatment of the model physics than on the model resolution. Our WRF-Chem performance for rainfall diurnal cycle in this region is similar to previous convection-permitting WRF-Chem simulations (e.g., Barth et al., 2012). Additionally, the WRF-Chem predicted mean rainfall rates over low-precipitation regions (e.g., several Atlantic states) are higher than those based on the Stage IV and GPM rainfall products, which tend to overestimate precipitation at the low end (e.g., Nelson et al., 2016; Tan et al., 2016). Such positive model biases for low-precipitation regions have also been reported in Barth et al. (2012).

320 Overall, the SMAP DA broadly reduced surface SM at the model initial times (i.e., 00 UTC each day), except the coastal Texas regions and parts of Ohio and Florida (Figure 2e). Such changes in SM are consistent with the modeled daytime RH responses (Figure 3b), and are anti-correlated with the model responses in its averaged daytime T2 and PBLH fields (Figure 2f;3j), as well as their daily amplitudes (not shown in figures). In places, the daily maxima of WRF-Chem T2 were delayed by an hour or two when the SMAP DA was enabled (Figure 2h). The changes in WRF-Chem temperature gradients due to

325 the SMAP DA led to slight WS enhancements over many of the model grids (Figure 3f). On the 13-day timescale, the SMAP DA had less discernable impacts on rainfall, consistent with findings from Koster et al. (2010, 2011) and Huang et al. (2018). The SMAP DA impacts on mean rainfall rate and diurnal cycles show noisy patterns (Figure 4d;g;h), and positive and negative SM-precipitation relationships are both found. The spatial and temporal variability in these model sensitivities reflects the impacts of local hydrological regimes and their anomalies as well as moisture advection.

330 The inclusion of the SMAP DA did not dominantly improve or degrade the overall T2, RH and WS performance of WRF-Chem (e.g., Figures 2g;3d;3h, based on the root-mean-square error (RMSE) metric): i.e., improvements on T2, RH, and WS occurred in 47%, 51% and 52% of the model grids where observations are available, and the domain-wide mean RMSE changes for T2, RH, and WS are ~0 °K, -0.024%, and -0.005 ms^{-1}, respectively. This is qualitatively consistent with the findings in Huang et al. (2018) and Yin and Zhan (2018) for dense vegetation regions (i.e., green vegetation fraction >0.6),

335 based on RMSE and other evaluation metrics. Additionally, as discussed in Huang et al. (2018), unrealistic model representations of terrain height can pose challenges for evaluating the modeled surface weather fields with ground-based observations. The 12 km model grid used in this work well represents terrain height (i.e., |model-actual|<15 m) at over 70% of the model grids that have collocated observations, but at some locations the discrepancies between the model and actual terrain height exceed 100 m. Furthermore, human activities such as irrigation can significantly modify water budget and

340 land-atmosphere coupling strength over agricultural regions (e.g., Lu et al., 2017), but these were unmodeled (i.e., not accounted for) in the used modeling system. Observations from SMAP and other satellites are capable of detecting the signals of irrigation over the southeastern US (e.g., the circled regions in Figure 1c based on Ozdogan and Gutman (2008) and Zaussinger et al. (2019)) and other regions of the world. How irrigation patterns and scheduling, depending in part on the weather conditions, affected our WRF-Chem performance as well as the effectiveness of the SMAP bias correction and

345 DA are worth further investigations. In places, the changes in WRF-Chem rainfall patterns due to the SMAP DA are within

the discrepancies between the Stage IV and GPM rainfall products. A better understanding of the uncertainty associated with these two used rainfall products can benefit the assessment of SM DA impacts on the model's precipitation performance.

The spatial patterns of evaporative fraction (defined as: latent heat/(latent heat+sensible heat)) follow those of SM and RH, with the maxima (>0.75) seen in the Lower Mississippi River region and smaller values (<0.65) in the dry Atlantic states and
350 some parts of the southern Great Plains (Figure 5a-b). Note that the absolute latent and sensible heat fluxes can differ significantly at locations with similar evaporative fraction values (Figure S3). The WRF-Chem based evaporative fraction shows similar spatial gradients but is overall negatively biased (Figure 5c). The changes in WRF-Chem evaporative fraction due to the SMAP DA are spatially correlated with the surface moisture changes (Figure 2e;3b;5d). As a result, the model performance of evaporative fraction was only improved over some of the regions where it was increased by the SMAP DA.
355 It is found that the SMAP DA impacts on model performance are not universally consistent for energy fluxes and land/atmosphere states. This can be explained by the fact that this used modeling system has shortcomings in representing SM-flux coupling and/or the relationships between moisture/heat fluxes and the atmospheric weather which need to be clearly identified and corrected. Future efforts should be devoted to: evaluation of additional flux variables (e.g., runoff, radiation), applications using other LSMs (e.g., the Noah-Multiparameterization) together with multivariate land DA, and
360 utilization of alternative WRF inputs and physics configurations.

The WRF-Chem modeled weather states were also evaluated with ACT-America aircraft observations at various altitudes. Along the flight paths, the observed air temperature and water vapor mixing ratios decrease with altitude. The modeled air temperature and humidity as well as their responses to the SMAP DA vary in space and time. In general, these responses are particularly strong near the surface. Under stormy weather conditions on 16, 20, 21 of August 2016, the maximum changes
365 in air temperature and humidity in the free troposphere exceeded 2.5 °K and 2 g/kg, respectively (Figure 6c;f). Corresponding to these changes, the SMAP DA modified the RMSEs of WRF-Chem air temperature and/or water vapor by over 5% for several individual flights and overall reduced the RMSEs of these model variables by ~0.7% and ~1.6%, respectively (Figures 7).

3.3 SMAP DA impacts on surface O_3 concentrations

370 The changes in the above-described meteorological variables (e.g., air temperature, RH, WS, PBLH) due to the SMAP DA alter various atmospheric processes which can have mixed impacts on surface O_3 concentrations. For example, warmer environments promote biogenic VOC and soil NO emissions as well as accelerate chemical reactions. Faster winds and thickened PBL dilute air pollutants including O_3 and its precursors, and therefore reduce O_3 destruction via titration (i.e., $O_3+NO \rightarrow O_2+NO_2$) as well as photochemical production of O_3. The changes in wind vectors affect pollutants' concentrations
375 in downwind regions. Water vapor mixing ratios perturb O_3 photochemical production and loss via affecting the HO_x cycle. Also, higher RH often has relevance with cloud abundance and solar radiation and therefore slow down the photochemical

processes (Camalier et al., 2007). Additionally, chemical loss via stomatal uptake may be slower under lower-SM/humidity, higher-temperature conditions, and nonstomatal uptake also varies with meteorology. These processes, however, may not be realistically represented by the Wesely dry deposition scheme (Section 2.1) used in this study.

380   Figure 8a-b compare the observed and WRF-Chem base case daytime surface O_3 during 16-28 August 2016, and the SMAP DA impacts on daytime surface O_3 are shown in Figure 8c. Low-to-moderate O_3 pollution levels are seen over most areas within the model domain, except the Atlantic states due to the influences of frequent air stagnation, warm and dry conditions. Period-mean daytime surface O_3 responses to the SMAP DA are overall slightly positive, but exceeded 2 ppbv in places. The O_3 changes show strong spatial correlations with those of T2 and PBLH (Figure 2f;3j), which are anti-correlated with the
385   surface humidity responses (Figure 2e;3b). The maximum impacts of SMAP DA on daily daytime surface O_3 exceeded 4 ppbv on most of the days during 16-28 August 2016 (Figure 9a). On almost all days, the O_3 sensitivities are moderately correlated with the daytime T2 changes (blue text in Figure 9a). The period-mean WRF-Chem surface MDA8 and its response to the SMAP DA (Figure 10a-b) show similar spatial patterns to those of the modeled surface daytime O_3, but are of slightly higher magnitudes. Enhanced biogenic isoprene and soil NO emissions (Figure 3k-n and Figure S4), especially
390   for the regions with elevated emissions (e.g., the Missouri Ozarks for isoprene and agricultural land for soil NO), as well as accelerated photochemical reactions were the major causes of such changes in surface daytime-average and MDA8 O_3. MEGAN's limitations in representing biogenic VOC emission responses to drought may have had minor impacts on most of the high-isoprene-emission regions which were not affected by drought during this period. Uncertainty in the modeled soil NO emissions and their responses to the SMAP DA may be larger over high-temperature cropland regions which needs
395   further investigations accounting for the influences of SM and fertilization conditions. The deposition velocities of O_3 and its related chemical species also responded to the SMAP DA, with the O_3 deposition velocity changes estimated to be the most important to the modeled O_3 concentrations according to previous studies (e.g., Baublitz et al., 2020). The modeled daytime O_3 deposition velocity responses to the SMAP DA (Figure 3o-p and Figure S4) are found anti-correlated with those in the surface temperature. Note that these deposition results are based on the Wesely scheme in which the SM influence on
400   stomatal resistance is omitted. If a SM limitation factor (details in Figure S1 caption) was included in the calculations, the modeled deposition velocities would respond more strongly to the SMAP DA. Including such a SM limitation factor, however, would not necessarily improve the modeled deposition velocities in part due to the uncertainty in the model's LULC input and the prescribed seasonal- and LULC-dependent constants in the used Wesely scheme.

   The SMAP DA improved surface MDA8 at 42% and 51% of the model grids where AQS and/or CASTNET observations are available, respectively. The domain-wide mean MDA8 RMSE changes due to the SMAP DA are 0.058 ppbv and 0.007
405   ppbv referring to gridded AQS and CASTNET O_3 observations, respectively. As summarized in Table 2, after enabling the SMAP DA, the number of grids with O_3 exceedance false alarms (i.e., WRF-Chem MDA8 O_3>70 ppbv but the observed MDA8 O_3<=70 ppbv) remained the same, except that this number dropped on 18 August and increased on 26 August. Such

O$_3$ performance changes in response to the SMAP DA are overall less desirable than those in the weather fields. This can be

410   explained by the fact that many other factors, such as the quality of the anthropogenic emission input of WRF-Chem, also

affected the model's surface O$_3$ performance. Figures 10c;f and 9b show that using NEI 2016 beta anthropogenic emissions

instead of the outdated NEI 2014 resulted in notable reductions in surface daytime-average and MDA8 O$_3$ across the model

domain. These reductions lowered the modeled surface O$_3$ biases by up to ~4 ppbv and reduced the number of grids with O$_3$

exceedance false alarms on 7 out of the 13 days (Table 2). Improving the modeled weather fields via the SMAP DA would

415   more clearly improve the model's O$_3$ performance if the uncertainty of NEI 2016 beta and other inputs as well as the model

parameterizations (e.g., chemical mechanism, natural emission, photolysis and deposition schemes) is reduced.

It is noticed that daytime surface O$_3$ fields from the global CAMS and AM4 modeling systems are overall higher than those

simulated by WRF-Chem (Figure 8b;d;e). One of the reasons is that stratosphere-troposphere exchanges are better

represented in these two global models. According to AM4's stratospheric tracer, during the study period, the stratospheric

420   O$_3$ influences on daytime surface O$_3$ range from <2 ppbv in the southern Great Plains (storm-affected regions) to 6-7 ppbv

around Kansas and the Atlantic Ocean. Note that although AM4 provides a broad overview of the areas strongly impacted by

stratospheric air, fine-scale features associated with stratospheric intrusions may be missing from this coarse-resolution

simulation (Lin et al., 2012; Ott et al., 2016). In the used WRF-Chem system, which has only tropospheric chemistry, the

representation of stratospheric influences only depends on the quality of the model's chemical LBCs. This representation

425   may be improved by adding accurate, time-varying chemical upper boundary conditions, e.g., downscaled from a well-

performed global model simulation. Such an update, however, is expected to increase the modeled surface O$_3$ (e.g., Figure 3

in Huang et al., 2013, based on a different regional air quality model). For regions where modeled surface O$_3$ is already

positively biased, stronger efforts to address other sources of model errors would be needed to achieve desirable surface O$_3$

performance.

430   **3.4 SMAP DA impacts on O$_3$ at various altitudes**

The SMAP DA impacts on WRF-Chem modeled chemical fields are also investigated at a wide range of altitudes. Figure 6g-

l compare the observed and WRF-Chem base case O$_3$ and CO concentrations along nine ACT-America flights in August

2016, as well as the SMAP DA impacts on WRF-Chem results at these sampling locations. The observed and modeled CO

vertical profiles show strong day-by-day variability, with near-surface concentrations ranging from 60 to 170 ppbv and

435   elevated concentrations aloft (<600 hPa) occurring on 16, 20, 21 of August when aircraft measurements were taken under

stormy weather conditions. In general, the observed and modeled O$_3$ increase with altitude. WRF-Chem fairly well captured

the magnitudes of the near-surface O$_3$ concentrations but underpredicted O$_3$ in the free troposphere. Overall, the modeled

trace gas concentrations reacted to the SMAP DA most strongly near the surface. Under stormy weather conditions, the

changes in modeled CO and O$_3$ approach 15 ppbv and 10 ppbv, respectively. The SMAP DA impacts on modeled CO and O$_3$

440   RMSEs are overall close to neutral (|ΔRMSE|<0.5%) but over 2% during selected flights (Figures 7). Similar to the

evaluation results for surface weather and O_3 fields, the O_3 performance changes by the SMAP DA are less desirable than those in the weather fields.

To help better understand SM controls on upper tropospheric O_3 chemistry, Figure 11 shows the period-mean (16-28 August 2016) daytime O_3, CO, and NO_2 at ~400 hPa from the WRF-Chem base simulation, as well as the SMAP DA impacts on

445 these model fields. The daily daytime O_3 responses to the SMAP DA at ~400 hPa are presented in Figure 9c. Elevated WRF-Chem O_3 concentrations (>70 ppbv) are seen near the center of the upper-tropospheric anticyclone (Figure S2, right), which circulated the lifted pollutants and promoted in-situ chemical production. The SMAP DA modified the period-mean daytime O_3 by up to >1 ppbv, and its impact on daytime O_3 on individual days during the study period occasionally exceeded 10 ppbv, which is larger than its maximum impact on the daily daytime surface O_3 (Figure 9a;c). As indicated by the modeled

450 CO and NO_2 responses to the SMAP DA, O_3 distributions in the upper troposphere and their responses to the SMAP DA are partially controlled by atmospheric transport and rapid in-situ chemical production of O_3 from lightning NO and other emissions, both of which are sensitive to SM. Note that although CO and NO_2 are used here primarily as a tracer of transport and an indicator of lightning production, respectively, lightning emissions can modify CO lifetimes, and atmospheric transport can also affect NO_2.

455 Similar to the O_3 conditions at the surface, at ~400 hPa, the WRF-Chem simulated daytime O_3 concentrations are lower than the global CAMS and AM4 results (Figure 11a-b) as well as the ACT-America aircraft measurements (Figure 6g-h), by up to tens of ppbv. The AM4 stratospheric tracer suggests 5-17 ppbv of stratospheric influences on period-mean O_3 at these altitudes (Figure 11c), which again helps identify the shortcoming of WRF-Chem in representing stratosphere-troposphere exchanges. Applying accurate, time-varying chemical upper boundary conditions in future works can help better assess the

460 SMAP DA impact on O_3 performance in the upper troposphere and improve the understanding of upper tropospheric chemistry.

3.5 SMAP DA versus anthropogenic emission perturbation impacts on tropospheric O_3

Perturbing anthropogenic emissions was a major approach implemented in the HTAP Phases 1 and 2 (HTAP1 and HTAP2) multi-model experiments to quantify how emission changes in one given region of the world affect air pollution in other

465 regions of the world (Fiore et al., 2009; Huang et al., 2017a). Based on HTAP1 multi-model (at horizontal resolutions ranging from 1°×1° to 5°×5°) estimates for August 2001, European surface O_3 decreased by ~0.35 ppbv in response to a 20% reduction in North American anthropogenic emissions (Fiore et al., 2009). Using HTAP2 configurations, a 0.7°×0.7° Composition-Integrated Forecasting System (C-IFS, which is the forecast model of CAMS) estimated that, in August 2010, ~400 hPa and surface O_3 concentrations over the southeastern US were reduced by 0.7-1.5 ppbv and >2 ppbv, respectively,

470 in response to a 20% reduction in North American anthropogenic emissions. Such an emission perturbation also reduced

European ~400 hPa and surface O_3 by 0.4-0.7 ppbv (i.e, ~1/3-1/2 of the 0.7-1.5 ppbv changes in the southeastern US due to dilution and chemical loss along the great transport distance) and 0.1-0.5 ppbv, respectively.

Based on our WRF-Chem base and "NEI14" simulations, we quantified the impact of updating anthropogenic emissions from NEI 2014 to NEI 2016 beta (<20% of change for most species as introduced in Section 2.1) on daytime O_3 export from
475 the southeastern US. Although skewed to negative values, the O_3 changes related to the NEI emission update show comparable magnitudes with those due to the SMAP DA at ~400 hPa: i.e., mostly within ±10 ppbv and ±1.5 ppbv at daily and 13-day timescales, respectively (Figure 9c-d;11g;12b). This suggests that the SMAP DA and the US EPA estimated anthropogenic emission change from 2014 to 2016 over the southeastern US could have similar levels of impact on O_3 in Europe. Referring to the C-IFS HTAP2 sensitivity simulation results, at ~400 hPa, the impacts on European O_3 may be 1/3-
480 1/2 of the O_3 changes in the southeastern US, and at the surface, the impacts may be within ±0.5 ppbv. Such estimations based on results from different modeling systems for different time periods need further evaluation.

This analysis highlights the important role of SM in quantifying pollutants' source-receptor relationships between the US and Europe. It also emphasizes that using outdated anthropogenic emissions in WRF-Chem would lead to inaccurate assessments of the SMAP DA impacts on the model performance of O_3 and other air pollutants over a broad region.

485 ### 3.6 Evaluation of NEI 2014 using WRF-Chem simulations and SEAC[4]RS observations

We compared NO_2, HCHO and CO from two 25 km WRF-Chem simulations (i.e., the "SEACf" and "SEACa" cases in Table 1) with aircraft observations during six SEAC[4]RS flights in August 2013 (Figure S5). Such comparisons help evaluate the emissions of O_3 precursors from various (e.g., NEI 2014 anthropogenic, lightning and biogenic) sources as well as how the model representation of land-atmosphere interactions can affect such emission assessments. It is shown that in case
490 "SEACf", WRF-Chem reproduced the overall vertical gradients of the observed chemicals, except that at this resolution it had difficulty in capturing urban plumes (e.g., for where the observed NO_2 >4 ppbv). This suggests that emissions of major O_3 precursors are moderately well represented in the used WRF-Chem system. The strongest changes in modeled NO_2, HCHO, and CO by assimilating the CCI SM are ~2 ppbv, ~3 ppbv, and ~25 ppbv, respectively, all occurring near the surface (>700 hPa). In the upper troposphere, the SM DA reduced the modeled NO_2 by up to ~0.5 ppbv (at ~400 hPa) and enhanced
495 the modeled CO by up to ~6 ppbv (at ~200 hPa). These changes led to better model agreements with the observations, indicating that assimilating the CCI SM likely improved the model treatment of lightning production and convective transport. As the SM DA modified the mismatches between the modeled and the observed trace gas concentrations, it is suggested that accurate representations of land-atmosphere interactions can benefit more rigorous evaluation and improvement of emissions using observations. Additionally, aircraft observations show robustness in aiding the evaluation of
500 the emissions of O_3 precursors from various sources, and therefore continuing to make rich and detailed observations like

those would be helpful for evaluating and improving newer/future versions of emission estimates as well as the model representations of land-atmosphere interactions.

4 Summary and suggestions on future directions

This study focused on evaluating SMAP SM DA impacts on coupled WRF-Chem weather and air quality modeling over the
505   southeastern US during the ACT-America campaign in August 2016. The impacts of SMAP DA on WRF-Chem modeled daytime RH as well as evaporative fraction were qualitatively consistent with the changes in the model's initial SM states, which were anti-correlated with the modeled daytime surface T2 and PBLH changes. The DA impacts on WRF-Chem performance of weather states and energy fluxes showed strong spatiotemporal variability, and many factors such as dense vegetation, complex terrain, and unmodeled processes such as water use from human activities (e.g., irrigation) may have
510   impacted the effectiveness of the DA. Overall, the modeled T2, RH, and WS performance was improved by the DA in 47%, 51% and 52% of the grids where observations were available. Referring to ACT-America aircraft observations on nine flight days, the DA reduced the RMSEs of WRF-Chem air temperature and water vapor by ~0.7% and ~1.6%, respectively. The overall DA impact on the modeled rainfall was less discernable, within the discrepancies between two rainfall evaluation products in places. The DA impacts on model performance were not consistent for energy flux partitioning and
515   land/atmosphere states everywhere, suggesting that the used modeling system had shortcomings in representing SM-flux coupling and/or the relationships between moisture/heat fluxes and the atmospheric weather which need to be clearly identified and corrected. Future efforts should focus on: 1) evaluation of additional flux variables (e.g., runoff, radiation); 2) applications using other LSMs along with multivariate land DA; and 3) utilization of alternative LIS/WRF configurations, including adding irrigation processes to the modeling system and performing convection-permitting simulations with the
520   assimilation of various kinds of high-resolution land products. Additionally, improving bias correction methods (e.g., also matching higher moments of the LSM and satellite SM climatology) and practicing the assimilation of SMAP Level 1 brightness temperature alone or in combination with atmospheric observations will be needed.

The SMAP DA impact on WRF-Chem surface daytime-average and MDA8 O_3 were strongly correlated with the changes in daytime T2 and PBLH, which were anti-correlated with the daytime surface humidity changes. Such changes in surface O_3
525   were mainly due to enhanced biogenic isoprene and soil NO emissions as well as accelerated photochemical reactions in response to the DA, and the changes in the modeled dry deposition fields also played a role. The SMAP DA impacts on modeled O_3 along the ACT-America flight paths were particularly strong (i.e., approaching 10 ppbv) under stormy weather conditions. The WRF-Chem O_3 performance change in response to the DA was overall less desirable than those in the weather fields. This in part was because many other factors, such as the model representations of anthropogenic emissions
530   and stratosphere-troposphere exchanges, also affected the model's surface O_3 performance.

We showed that at ~400 hPa, elevated O_3 concentrations were modeled near the center of the upper tropospheric anticyclone. The modeled O_3 was negatively biased, mainly resulting from the poor representation of stratosphere-troposphere exchanges by WRF-Chem. The impact of SMAP DA on upper tropospheric O_3 was partially via altering atmospheric transport and in-situ chemical production of O_3 from lightning NO and other emissions. We also presented that the impacts of DA and an

535 emission update from NEI 2014 to NEI 2016 beta on WRF-Chem modeled upper tropospheric O_3 had comparable magnitudes. As indicated by HTAP2 global model sensitivity simulations, a reduction in North American anthropogenic emissions would be beneficial for mitigating European O_3 pollution. Therefore, our analysis highlighted the important role of SM in quantifying the pollutants' source-receptor relationships between the US and Europe. It also emphasized that using up-to-date anthropogenic emissions in WRF-Chem would be necessary for accurately assessing SM DA impacts on the

540 model performance of O_3 and other air pollutants over a broad region. Continuing to improve NEI 2016 beta and any newer versions of emission estimates, as well as the parameterizations and other inputs of the models, is strongly encouraged. Such efforts can benefit from rich, detailed, high-accuracy observations, such as those taken during airborne field campaigns.

This study is a critical first step towards using satellite SM products to help improve the simulated weather and chemistry

545 fields in models that are widely-used for air quality research and forecasting, as well as policy-relevant assessments. It is necessary to clarify that in this study the SMAP DA influenced the WRF-Chem modeled O_3 mainly via changing the model's weather fields that drove its chemistry calculations online. The parameterizations for biogenic emissions and dry deposition in the standard WRF-Chem model were not modified in this study to realistically reflect the impacts of water availability. Ozone damage to vegetation was not modeled in this work, which was expected to only have minor impacts on

550 these half-month-long simulations. Reducing these limitations in WRF-Chem and other models' parameterizations (e.g., Hudman et al., 2012; Val Martin et al., 2014; Sadiq et al., 2017; Jiang et al., 2018; Clifton et al., 2020) are important to further improving the modeled chemical fields via applying the SM DA at various scales. Using dynamic vegetation models (available in the Noah-Multiparameterization LSM) along with additional process-based (e.g., chemical fluxes, stomatal behaviors) measurements and laboratory experiments would be necessary for improving some of these parameterizations,

555 and these will be experimented in a follow-up study. Community efforts such as the ongoing Air Quality Model Evaluation International Initiative Phase 4 experiment (https://aqmeii.jrc.ec.europa.eu/phase4.html) would also be greatly beneficial. High-quality weather input is a requirement for rigorous evaluations of any set of these parameterizations.

Code and data availability

The standalone LIS is accessible at: https://lis.gsfc.nasa.gov. LIS/WRF-Chem coupling is facilitated in the NASA-Unified

560 WRF system (https://nuwrf.gsfc.nasa.gov). The global C-IFS simulations for HTAP2 are available at the AeroCom database. Observations and observation-derived data products used in this work can be found at: https://nsidc.org/data/smap/smap-data.html; https://www.esa-soilmoisture-cci.org; https://www.air.larc.nasa.gov/index.html; https://www.epa.gov/aqs;

https://www.epa.gov/castnet; https://rda.ucar.edu/datasets/ds461.0; https://fluxnet.fluxdata.org; http://www.fluxcom.org; https://www.emc.ncep.noaa.gov/mmb/ylin/pcpanl/stage4; and https://pmm.nasa.gov/data-access/downloads/gpm.

Author contributions

MH led the design and execution of the study as well as the paper writing. JHC, JPD, GRC, and KWB contributed to the field campaign data collection and/or analysis. GRC, KWB, SVK and XZ contributed to the modeling and/or DA work. All authors helped finalize the paper.

Competing interests

The authors declare that they have no conflict of interest.

Acknowledgements

We thank the ACT-America flight, instrument and data management teams, and the ACT-America Principal Investigator, Kenneth Davis (Penn State), for designing and conducting the NASA B200 flights, as well as helping with the analysis. We also thank the SEAC^{4}RS instrument teams (PIs: Thomas Ryerson, NOAA/ESRL; Ronald Cohen, UC Berkeley; Alan Fried, CU-Boulder; Thomas Hanisco, NASA GSFC; Glenn Diskin, NASA LaRC; and Armin Wisthaler, University of Innsbruck) and FLUXNET PIs for sharing their measurements. The ECMWF CAMS and GFDL AM4 (contacts: Meiyun Lin, Princeton; Alex Zhang, now at Penn State) modeling teams are acknowledged for generating the global model outputs used in this study. The global C-IFS simulations for HTAP2 were conducted by Johannes Flemming (ECMWF). Sophia Walther (MPI-BGC), Kazuyuki Miyazaki (JPL/Caltech), and Li Fang (UMD) provided datasets that are not directly related to this study but informative. NASA SUSMAP sponsorship for this work as well as NASA's high-end computing systems and services is acknowledged. The ACT-America project is a NASA Earth Venture Suborbital 2 project funded by NASA's Earth Science Division (Grant NNX15AG76G to Penn State).

References

Anav, A., Proietti, C., Menut, L., Carnicelli, S., De Marco, A., and Paoletti, E.: Sensitivity of stomatal conductance to soil moisture: implications for tropospheric ozone, Atmos. Chem. Phys., 18, 5747–5763, doi:10.5194/acp-18-5747-2018, 2018.

Avnery, S., Mauzerall, D. L., Liu, J., and Horowitz, L. W.: Global Crop Yield Reductions due to Surface Ozone Exposure: 1. Year 2000 Crop Production Losses and Economic Damage, doi:10.1016/j.atmosenv.2010.11.045, Atmos. Environ., 45, 2284–2296, 2011.

590

Baublitz, C. B., Fiore, A. M., Clifton, O. E., Mao, J., Li, J., Correa, G., Westervelt, D. M., Horowitz, L. W., Paulot, F., and Williams, A. P.: Sensitivity of Tropospheric Ozone Over the Southeast USA to Dry Deposition, Geophys. Res. Lett., 47, e2020GL087158, doi:10.1029/2020GL087158, 2020.

595   Barth, M. C., Lee, J., Hodzic, A., Pfister, G., Skamarock, W. C., Worden, J., Wong, J., and Noone, D.: Thunderstorms and upper troposphere chemistry during the early stages of the 2006 North American Monsoon, Atmos. Chem. Phys., 12, 11003–11026, doi:10.5194/acp-12-11003-2012, 2012.

Bertschi, I. T. and Jaffe, D. A.: Long-range transport of ozone, carbon monoxide, and aerosols to the NE Pacific troposphere
600   during the summer of 2003: Observations of smoke plumes from Asian boreal fires, J. Geophys. Res., 110, D05303, doi:10.1029/2004JD005135, 2005.

Betts, R. A., Ball, J. H., Beljaars, A. C. M., Miller, M. J., and Viterbo, P.: The land-surface-atmosphere interaction: A review based on observational and global modeling perspectives, J. Geophys. Res., 101, 7209–7225, doi:10.1029/95JD02135, 1996.

605

Boccippio, D. J., Cummins, K. L., Christian, H. J., and Goodman, S. J.: Combined Satellite- and Surface-Based Estimation of the Intracloud–Cloud-to-Ground Lightning Ratio over the Continental United States, Mon. Weather Rev., 129, 108–122, doi:10.1175/1520-0493(2001)129<0108:CSASBE>2.0.CO;2, 2001.

610   Bowman, K. W., Shindell, D. T., Worden, H. M., Lamarque, J. F., Young, P. J., Stevenson, D. S., Qu, Z., de la Torre, M., Bergmann, D., Cameron-Smith, P. J., Collins, W. J., Doherty, R., Dalsøren, S. B., Faluvegi, G., Folberth, G., Horowitz, L. W., Josse, B. M., Lee, Y. H., MacKenzie, I. A., Myhre, G., Nagashima, T., Naik, V., Plummer, D. A., Rumbold, S. T., Skeie, R. B., Strode, S. A., Sudo, K., Szopa, S., Voulgarakis, A., Zeng, G., Kulawik, S. S., Aghedo, A. M., and Worden, J. R.: Evaluation of ACCMIP outgoing longwave radiation from tropospheric ozone using TES satellite observations, Atmos.
615   Chem. Phys., 13, 4057–4072, doi:10.5194/acp-13-4057-2013, 2013.

Brown-Steiner, B. and Hess, P.: Asian influence on surface ozone in the United States: A comparison of chemistry, seasonality, and transport mechanisms, J. Geophys. Res., 116, D17309, doi:10.1029/2011JD015846, 2011.

620 Bucsela, E., Pickering, K. E., Allen, D. J., Holzworth, R. H., and Krotkov, N. A.: Mid-latitude lightning NO_x production efficiency inferred from OMI and WWLLN data, J. Geophys. Res. Atmos., doi:10.1029/2019JD030561, 2019.

Camalier, L., Cox, W., and Dolwick, P.: The effects of meteorology on ozone in urban areas and their use in assessing ozone trends, Atmos. Environ., 41, 7127–7137, doi:10.1016/j.atmosenv.2007.04.061, 2007.

625

Charusombat, U., Niyogi, D., Kumar, A., Wang, X., Chen, F., Guenther, A., Turnipseed, A., and Alapaty, K.: Evaluating a new deposition velocity module in the Noah land-surface model, Bound.- Lay. Meteorol., 137, 271–290, 2010.

Chen, F. and Dudhia, J.: Coupling an advanced land surface hydrology model with the Penn State-NCAR MM5 modeling
630 system. Part I: Model implementation and sensitivity, Mon. Weather Rev., 129, 569–585, doi:10.1175/1520-0493(2001)129<0569:CAALSH>2.0.CO;2, 2001.

Cioni, G. and Hohenegger, C.: Effect of soil moisture on diurnal convection and precipitation in Large-Eddy Simulations, J. Hydrometeorol., 18, 1885–1903, doi:10.1175/JHMD-16-0241.1, 2017.

635

Clifton, O. E., Paulot, F., Fiore, A. M., Horowitz, L. W., Correa, G., Baublitz, C. B., Fares, S., Goded, I., Goldstein, A. H., Gruening, C., Hogg, A. J., Loubet, B., Mammarella, I., Munger, J. W., Neil, L., Stella, P., Uddling, J., Vesala, T., and Weng, E: Influence of dynamic ozone dry deposition on ozone pollution, J. Geophys. Res. Atmos., 125, e2020JD032398, doi:10.1029/2020JD032398, 2020.

640

Coates, J., Mar, K. A., Ojha, N., and Butler, T. M.: The influence of temperature on ozone production under varying NO_x conditions–a modelling study, Atmos. Chem. Phys., 16, 11601–11615, doi:10.5194/acp-16-11601-2016, 2016.

Cohen, A. J., Brauer, M., Burnett, R., Anderson, H. R., Frostad, J., Estep, K., Balakrishnan, K., Brunekreef, B., Dandona, L.,
645 Dandona, R., Feigin, V., Freedman, G., Hubbell, B., Jobling, A., Kan, H., Knibbs, L., Liu, Y., Martin, R., Morawska, L., Pope, C. A., Shin, H., Straif, K., Shaddick, G., Thomas, M., van Dingenen, R., van Donkelaar, A., Vos, T., Murray, C. J. L., and Forouzanfar, M. H.: Estimates and 25-year trends of the global burden of disease attributable to ambient air pollution: an analysis of data from the Global Burden of Diseases Study 2015, Lancet, 389, 1907–1918, doi:10.1016/S0140-6736(17)30505-6, 2017.

650

Collow, T. W., Robock, A., and Wu, W.: Influences of soil moisture and vegetation on convective precipitation forecasts over the United States Great Plains, J. Geophys. Res. Atmos., 119, 9338–9358, doi:10.1002/2014JD021454, 2014.

Cooper, O. R., Trainer, M., Thompson, A. M., Witte, J. C., Oltmans, S. J., Morris, G., Pickering, K. E., Crawford, J. H.,
655   Chen, G., Cohen, R. C., Bertram, T. H., Wooldridge, P., Perring, A., Brune, W. H., Merrill, J., Moody, J. L., Tarasick, D.,
Nédélec, P., Forbes, G., Newchurch, M. J., Schmidlin, F. J., Johnson, B. J., Turquety, S., Baughcum, S. L., Ren, X.,
Fehsenfeld, F. C., Meagher, J. F., Spichtinger, N., Brown, C. C., McKeen, S. A., McDermid, I. S., and Leblanc, T.: Large
upper tropospheric ozone enhancements above midlatitude North America during summer: In situ evidence from the IONS
and MOZAIC ozone measurement network, J. Geophys. Res., 111, D24S05, doi:10.1029/2006JD007306, 2006.
660

Cooper, O. R., Trainer, M., Thompson, A. M., Oltmans, S. J., Tarasick, D. W., Witte, J. C., Stohl, A., Eckhardt, S.,
Lelieveld, J., Newchurch, M. J., Johnson, B. J., Portmann, R. W., Kalnajs, L., Dubey, M. K., Leblanc, T., McDermid, I. S.,
Forbes, G., Wolfe, D., Carey-Smith, T., Morris, G. A., Lefer, B., Rappenglück, B., Joseph, E., Schmidlin, F., Meagher, J.,
Fehsenfeld, F. C., Keating, T. J., Van Curen, R. A., and Minschwaner, K.: Evidence for a recurring eastern North America
665   upper tropospheric ozone maximum during summer, J. Geophys. Res. Atmos., 112, d23304, doi:10.1029/2007JD008710,
2007.

Cooper, O. R., Eckhardt, S., Crawford, J. H., Brown, C. C., Cohen, R. C., Bertram, T. H., Wooldridge, P., Perring, A.,
Brune, W. H., Ren, X., Brunner, D., and Baughcum, S. L.: Summertime buildup and decay of lightning NO_x and aged
670   thunderstorm outflow above North America, J. Geophys. Res. Atmos., 114, d01101, doi:10.1029/2008JD010293, 2009.

Cooper, O. R., Parrish, D. D., Ziemke, J., Balashov, N. V., Cupeiro, M., Galbally, I. E., Gilge, S., Horowitz, L., Jensen, N.
R., Lamarque, J.-F., Naik, V., Oltmans, S. J., Schwab, J., Shindell, D. T., Thompson, A. M., Thouret, V., Wang, Y. and
Zbinden, R. M.: Global distribution and trends of tropospheric ozone: An observation-based review, Elem. Sci. Anth., 2,
675   000029, doi:10.12952/journal.elementa.000029, 2014.

Darmenov, A., and da Silva, A.: The Quick Fire Emissions Dataset (QFED): Documentation of versions 2.1, 2.2 and 2.4.
NASA Technical Report Series on Global Modeling and Data Assimilation, NASA TM-2015-104606/Volume 38,
http://gmao.gsfc.nasa.gov/pubs/docs/Darmenov796.pdf, 2015.
680

de Rosnay, P., Drusch, M., Vasiljevic, D., Balsamo, G., Albergel, C. and Isaksen, L.: A simplified Extended Kalman Filter
for the global operational soil moisture analysis at ECMWF, Q. J. R. Meteorol. Soc., 139,1199–1213, doi:10.1002/qj.2023,
2013.

685   Dickerson, R. R., Huffman, G. L., Luke, W. T., Nunnermacker, L. J., Pickering, K. E., Leslie, A. C., Lindsey, C. G., Slinn,
W. G. N., Kelly, T. J., Daum, P. H., Delany, A. C., Greenberg, J. P., Zimmerman, P. R., Boatman, J. F., Ray, J. D., and

Stedman, D. H.: Thunderstorms-An important mechanism in the transport of air pollutants, Science, 235, 460–464, doi:10.1126/science.235.4787.460, 1987.

690   Dirmeyer, P. A.: The terrestrial segment of soil moisture-climate coupling, Geophys. Res. Lett., 38, L16702, doi:10.1029/2011GL048268, 2011.

Dirmeyer, P. A., Cash, B. A., Kinter III, J. L., Jung, T., Marx, L., Satoh, M., Stan, C., Tomita, H., Towers, P., Wedi, N., Achuthavarier, D., Adams, J. M., Altshuler, E. L., Huang, B., Jin, E. K., and Manganello, J.: Simulating the diurnal cycle of

695   rainfall in global climate models: resolution versus parameterization, Clim. Dyn., 39, 399–418, doi:10.1007/s00382-011-1127-9, 2012.

Dirmeyer, P. A., Jin, Y., Singh, B., and Yan, X.: Evolving land-atmosphere interactions over North America from CMIP5 simulations, J. Clim., 26, 7313–7327, doi:10.1175/JCLI-D-12-00454.1, 2013.

700

Doherty, R. M., Wild, O., Shindell, D. T., Zeng, G., MacKenzie, I. A., Collins, W. J., Fiore, A. M., Stevenson, D. S., Dentener, F. J., Schultz, M. G., Hess, P., Derwent, R. G. and Keating, T. J.: Impacts of climate change on surface ozone and intercontinental ozone pollution: A multi-model study, J. Geophys. Res. Atmos., 118, 3744–3763, doi:10.1002/jgrd.50266, 2013.

705

Doherty, R. M.: Ozone Pollution from Near and Far, Nature Geosci., 8, 664–665, doi: 10.1038/ngeo2497, 2015.

Entekhabi, D., Njoku, E. G., O'Neill, P. E., Kellogg, K. H., Crow, W. T., Edelstein, W. N., Entin, J. K., Goodman, S. D., Jackson, T. J., Johnson, J., Kimball, J., Piepmeier, J. R., Koster, R. D., Martin, N., McDonald, K. C., Moghaddam, M.,

710   Moran, S., Reichle, R., Shi, J. C., Spencer, M. W., Thurman, S. W., Tsang, L., and van Zyl, J.: The Soil Moisture Active Passive (SMAP) Mission., Proc. IEEE, 98(5), 704–716, doi:10.1109/JPROC.2010.2043918, 2010.

Fast, J. D., Berg, L. K., Feng, Z., Mei, F., Newsom, R., Sakaguchi, K., and Xiao, H.: The impact of variable land-atmosphere coupling on convective cloud populations observed during the 2016 HI-SCALE field campaign, J. Adv. Model Earth, 11,

715   doi:10.1029/2019MS001727, 2019.

Finney, D. L., Doherty, R. M., Wild, O., Stevenson, D. S., Mackenzie I. A. and Blyth, A.: A projected decrease in lightning under climate change, Nat. Clim. Change, 8, 210–213, doi:10.1038/s41558-018-0072-6, 2018.

720   Fiore, A. M., Dentener, F. J., Wild, O., Cuvelier, C., Schultz, M. G., Hess, P., Textor, C., Schulz, M., Doherty, R. M., Horowitz, L. W., MacKenzie, I. A., Sanderson, M. G., Shindell, D. T., Stevenson, D. S., Szopa, S., Van Dingenen, R., Zeng, G., Atherton, C., Bergmann, D., Bey, I., Carmichael, G., Collins, W. J., Duncan, B. N., Faluvegi, G., Folberth, G., Gauss, M., Gong, S., Hauglustaine, D., Holloway, T., Isaksen, I. S. A., Jacob, D. J., Jonson, J. E., Kaminski, J. W., Keating, T. J., Lupu, A., Marmer, E., Montanaro, V., Park, R. J., Pitari, G., Pringle, K. J., Pyle, J. A., Schroeder, S., Vivanco, M. G., Wind, P.,

725   Wojcik, G., Wu, S., and Zuber, A.: Multimodel estimates of intercontinental source receptor relationships for ozone pollution, J. Geophys. Res., 114, D04301, doi:10.1029/2008JD010816, 2009.

Fishman, J., Belina, K. M., and Encarnación, C. H.: The St. Louis Ozone Gardens: Visualizing the Impact of a Changing Atmosphere, Bull. Am. Meteorol. Soc., 95, 1171–1176, doi:10.1175/bams-d-13-00009.1, 2014.

730

Fleming, Z. L., Doherty, R. M., von Schneidemesser, E., Malley, C. S., Cooper, O. R., Pinto, J. P., Colette, A., Xu, X., Simpson, D., Schultz, M. G., Lefohn, A. S., Hamad, S., Moolla, R., Solberg, S. and Feng, Z.: Tropospheric Ozone Assessment Report: Present-day ozone distribution and trends relevant to human health, Elem. Sci. Anth., 6,12, doi:10.1525/elementa.273, 2018.

735

Gevaert, A. I., Miralles, D. G., de Jeu, R. A. M., Schellekens, J., and Dolman, A. J.: Soil moisture-temperature coupling in a set of land surface models, J. Geophys. Res. Atmos., 123, 1481–1498, doi:10.1002/2017JD027346, 2018.

Grell, G., Peckham, S., Schmitz, R., McKeen, S., Frost, G., Skamarock, W., and Eder, B.: Fully coupled "online" chemistry

740   within the WRF model, Atmos. Environ., 39, 6957–6976, doi:10.1016/j.atmosenv.2005.04.027, 2005.

Grell, G. A. and Freitas, S. R.: A scale and aerosol aware stochastic convective parameterization for weather and air quality modeling, Atmos. Chem. Phys., 14, 5233–5250, doi:10.5194/acp-14-5233-2014, 2014.

745   Gruber, A., Scanlon, T., van der Schalie, R., Wagner, W., and Dorigo, W.: Evolution of the ESA CCI Soil Moisture climate data records and their underlying merging methodology, Earth Syst. Sci. Data, 11, 717–739, doi:10.5194/essd-11-717-2019, 2019.

Guenther, A., Karl, T., Harley, P., Wiedinmyer, C., Palmer, P. I., and Geron, C.: Estimates of global terrestrial isoprene

750   emissions using MEGAN (Model of Emissions of Gases and Aerosols from Nature), Atmos. Chem. Phys., 6, 3181–3210, doi:10.5194/acp-6-3181-2006, 2006.

Guillod, B. P., Orlowsky, B., Miralles, D. G., Teuling, A. J., and Seneviratne, S. I.: Reconciling spatial and temporal soil moisture effects on afternoon rainfall, Nat. Commun., 6, 6443, doi:10.1038/ncomms7443, 2015.

755

Guo, Z. and Dirmeyer, P. A.: Interannual variability of land-atmosphere coupling strength, J. Hydrometeorol., 14, 1636–1646, doi:10.1175/JHM-D-12-0171.1, 2013.

Harlan, S. L. and Ruddell, D. M.: Climate change and health in cities: impacts of heat and air pollution and potential co-
760 benefits from mitigation and adaptation, Curr. Opin. Env. Sust., 3, 126–134, doi:10.1016/j.cosust.2011.01.001, 2011.

Harris, N. R. P., Hassler, B., Tummon, F., Bodeker, G. E., Hubert, D., Petropavlovskikh, I., Steinbrecht, W., Anderson, J., Bhartia, P. K., Boone, C. D., Bourassa, A., Davis, S. M., Degenstein, D., Delcloo, A., Frith, S. M., Froidevaux, L., Godin-Beekmann, S., Jones, N., Kurylo, M. J., Kyrölä, E., Laine, M., Leblanc, S. T., Lambert, J.-C., Liley, B., Mahieu, E.,
765 Maycock, A., de Mazière, M., Parrish, A., Querel, R., Rosenlof, K. H., Roth, C., Sioris, C., Staehelin, J., Stolarski, R. S., Stübi, R., Tamminen, J., Vigouroux, C., Walker, K. A., Wang, H. J., Wild, J., and Zawodny, J. M.: Past changes in the vertical distribution of ozone – Part 3: Analysis and interpretation of trends, Atmos. Chem. Phys., 15, 9965–9982, doi:10.5194/acp-15-9965-2015, 2015.

770 Hess, P. G.: A comparison of two paradigms: The relative global roles of moist convective versus nonconvective transport, J. Geophys. Res., 110, D20302, doi:10.1029/2004JD005456, 2005.

Hogrefe, C., Isukapalli, S., Tang, X., Georgopoulos, P., He, S., Zalewsky, E., Hao, W., Ku, J., Key, T., and Sistla, G.: Impact of biogenic emission uncertainties on the simulated response of ozone and fine particulate matter to anthropogenic emission
775 reductions, J. Air Waste Manage., 61, 92–108, doi:10.3155/1047-3289.61.1.92, 2011.

Hohenegger, C., Brockhaus, P., Bretherton, C. S., and Schär, C.: The soil moisture-precipitation feedback in simulations with explicit and parameterized convection, J. Climate, 22, 5003–5020, 2009.

780 Huang, M., Carmichael, G. R., Adhikary, B., Spak, S. N., Kulkarni, S., Cheng, Y. F., Wei, C., Tang, Y., Parrish, D. D., Oltmans, S. J., D'Allura, A., Kaduwela, A., Cai, C., Weinheimer, A. J., Wong, M., Pierce, R. B., Al-Saadi, J. A., Streets, D. G., and Zhang, Q.: Impacts of transported background ozone on California air quality during the ARCTAS-CARB period – a multi-scale modeling study, Atmos. Chem. Phys., 10, 6947–6968, doi:10.5194/acp-10-6947-2010, 2010.

785 Huang, M., Carmichael, G. R., Chai, T., Pierce, R. B., Oltmans, S. J., Jaffe, D. A., Bowman, K. W., Kaduwela, A., Cai, C., Spak, S. N., Weinheimer, A. J., Huey, L. G., and Diskin, G. S.: Impacts of transported background pollutants on summertime

western US air quality: model evaluation, sensitivity analysis and data assimilation, Atmos. Chem. Phys., 13, 359–391, doi:10.5194/acp-13-359-2013, 2013.

790 Huang, M., Lee, P., McNider, R., Crawford, J., Buzay, E., Barrick, J., Liu, Y., and Krishnan, P.: Temporal and spatial variability of daytime land surface temperature in Houston: Comparing DISCOVER-AQ aircraft observations with the WRF model and satellites, J. Geophys. Res. Atmos., 121, 185–195, doi:10.1002/2015JD023996, 2016.

Huang, M., Carmichael, G. R., Pierce, R. B., Jo, D. S., Park, R. J., Flemming, J., Emmons, L. K., Bowman, K. W., Henze, D.
795 K., Davila, Y., Sudo, K., Jonson, J. E., Tronstad Lund, M., Janssens-Maenhout, G., Dentener, F. J., Keating, T. J., Oetjen, H., and Payne, V. H.: Impact of intercontinental pollution transport on North American ozone air pollution: an HTAP phase 2 multi-model study, Atmos. Chem. Phys., 17, 5721–5750, doi:10.5194/acp-17-5721-2017, 2017a.

Huang, M., Carmichael, G. R., Crawford, J. H., Wisthaler, A., Zhan, X., Hain, C. R., Lee, P., and Guenther, A. B.: Biogenic
800 isoprene emissions driven by regional weather predictions using different initialization methods: case studies during the SEAC^{4}RS and DISCOVER-AQ airborne campaigns, Geosci. Model Dev., 10, 3085–3104, doi:10.5194/gmd-10-3085-2017, 2017b.

Huang, M., Crawford, J. H., Diskin, G. S., Santanello, J. A., Kumar, S. V., Pusede, S. E., Parrington, M., and Carmichael, G.
805 R.: Modeling regional pollution transport events during KORUS-AQ: Progress and challenges in improving representation of land-atmosphere feedbacks, J. Geophys. Res. Atmos., 123, doi:10.1029/2018JD028554, 10732–10756, 2018.

Hudman, R. C., Russell, A. R., Valin, L. C., and Cohen, R. C.: Interannual variability in soil nitric oxide emissions over the United States as viewed from space, Atmos. Chem. Phys., 10, 9943–9952, doi:10.5194/acp-10-9943-2010, 2010.
810
Hudman, R. C., Moore, N. E., Mebust, A. K., Martin, R. V., Russell, A. R., Valin, L. C., and Cohen, R. C.: Steps towards a mechanistic model of global soil nitric oxide emissions: implementation and space based-constraints, Atmos. Chem. Phys., 12, 7779–7795, doi:10.5194/acp-12-7779-2012, 2012.

815 Huffman, G. J., Bolvin, D. T., Braithwaite, D., Hsu, K., Joyce, R., Kidd, C., Nelkin, E. J., Sorooshian, S., Tan, J., and Xie, P.: NASA Global Precipitation Measurement (GPM) Integrated Multi-satellitE Retrievals for GPM (IMERG), Algorithm Theoretical Basis Document (ATBD) Version 06, available at: https://pmm.nasa.gov/sites/default/files/document_files/IMERG_ATBD_V06.pdf (last access: March 2020), 2019.

820 Huijnen, V., Miyazaki, K., Flemming, J., Inness, A., Sekiya, T., and Schultz, M. G.: An intercomparison of tropospheric ozone reanalysis products from CAMS, CAMS-Interim, TCR-1 and TCR-2, Geosci. Model Dev., 13, 1513–1544, doi:10.5194/gmd-13-1513-2020, 2020.

Iacono, M. J., Delamere, J. S., Mlawer, E. J., Shephard, M. W., Clough, S. A., and Collins, W. D.: Radiative forcing by long-
825 lived greenhouse gases: Calculations with the AER radiative transfer models, J. Geophys. Res., 113, D13103, doi:10.1029/2008JD009944, 2008.

Intergovernmental Panel on Climate Change: Climate Change 2013: The Physical Science Basis. Contribution of Working Group I to the Fifth Assessment Report of the Intergovernmental Panel on Climate Change [Stocker, T.F., D. Qin, G.-K.
830 Plattner, M. Tignor, S.K. Allen, J. Boschung, A. Nauels, Y. Xia, V. Bex and P.M. Midgley (eds.)]. Cambridge University Press, Cambridge, United Kingdom and New York, NY, USA, https://www.ipcc.ch/report/ar5/wg1, 2013.

Jacob, D. and Winner, D. A.: Effect of climate change on air quality, Atmos. Env., 43, 51–63, doi:10.1016/j.atmosenv.2008.09.051, 2009.
835
Jiang, X., Guenther, A., Potosnak, M., Geron, C., Seco, R., Karl, T., Kim, S., Gu, L. and Pallardy, S.: Isoprene emission response to drought and the impact on global atmospheric chemistry, Atmos. Environ., 183, 69–83, doi:10.1016/j.atmosenv.2018.01.026, 2018.

840 Jung, M., Koirala, S., Weber, U., Ichii, K., Gans, F., Camps-Valls, G., Papale, D., Schwalm, C., Tramontana, G., and Reichstein, M.: The FLUXCOM ensemble of global land-atmosphere energy fluxes, Sci. Data, 6, 74, doi:10.1038/s41597-019-0076-8, 2019.

Karion, A., Sweeney, C., Wolter, S., Newberger, T., Chen, H., Andrews, A., Kofler, J., Neff, D., and Tans, P.: Long-term
845 greenhouse gas measurements from aircraft, Atmos. Meas. Tech., 6, 511–526, doi:10.5194/amt-6-511-2013, 2013.

Kelly, P. and Mapes, B.: Land surface heating and the North American monsoon anticyclone: Model evaluation from diurnal to seasonal., J. Clim., doi:10.1175/2010JCLI3332.1, 23, 4096–4106, 2010.

850 Kennedy, A. D., Dong, X., Xi, B., Xie, S., Zhang, Y., and Chen, J.: A Comparison of MERRA and NARR Reanalyses with the DOE ARM SGP Data, J. Climate, 24, 4541–4557, doi:10.1175/2011JCLI3978.1, 2011.

Koster, R. D., Dirmeyer, P. A., Guo, Z., Bonan, G., Chan, E., Cox, P., Gordon, C. T., Kanae, Shinjiro, Kowalczyk, E., Lawrence, D., Liu, P., Lu, C.-H., Malyshev, S., McAvaney, B., Mitchell, K., Mocko, D., Oki, T., Oleson, K., Pitman, A., Sud, Y. C., Taylor, C. M., Verseghy, D., Vasic, R., Xue, Y., and Yamada, T.: Regions of strong coupling between soil moisture and precipitation, Science, 305, 1138–1140, doi:10.1126/science.1100217, 2004.

Koster, R. D., Guo, Z., Dirmeyer, P. A., Bonan, G., Chan, E., Cox, P., Davies, H., Gordon, C. T., Kanae, S., Kowalczyk, E., Lawrence, D., Liu, P., Lu, C.-H., Malyshev, S., McAvaney, B., Mitchell, K., Mocko, D., Oki, T., Oleson, K. W., Pitman, A., Sud, Y. C., Taylor, C. M., Verseghy, D., Vasic, R., Xue, Y., and Yamada, T.: GLACE: The Global Land-Atmosphere Coupling Experiment. Part I: Overview, J. Hydrometeor., 7, 590–610, doi:10.1175/JHM510.1, 2006.

Koster, R. D., Mahanama, S. P. P., Yamada, T. J., Balsamo, G., Berg, A. A., Boisserie, M., Dirmeyer, P. A., Doblas-Reyes, F. J., Drewitt, G., Gordon, C. T., Guo, Z., Jeong, J.-H., Lawrence, D. M., Lee, W.-S., Li, Z., Luo, L., Malyshev, S., Merryfield, W. J., Seneviratne, S. I., Stanelle, T., van den Hurk, B. J. J. M., Vitart, F., and Wood, E. F.: Contribution of land surface initialization to subseasonal forecast skill: First results from a multi-model experiment, Geophys. Res. Lett., 37, L02402, doi:10.1029/2009GL041677, 2010.

Koster, R. D., Mahanama, S. P. P., Yamada, T. J., Balsamo, G., Berg, A. A., Boisserie, M., Dirmeyer, P. A., Doblas-Reyes, F. J., Drewitt, G., Gordon, C. T., Guo, Z., Jeong, J.-H., Lee, W.-S., Li, Z., Luo, L., Malyshev, S., Merryfield, W. J., Seneviratne, S. I., Stanelle, T., van den Hurk, B. J. J. M., Vitart, F., and Wood, E. F: The second phase of the Global Land-Atmosphere Coupling Experiment: Soil moisture contributions to subseasonal forecast skill, J. Hydrometeorol., 12, 805–822, doi:10.1175/2011JHM1365.1, 2011.

Kumar, S. V., Peters-Lidard, C. D., Tian, Y., Houser, P. R., Geiger, J., Olden, S., Lighty, L., Eastman, J. L., Doty, B., Dirmeyer, P., Adams, J., Mitchell, K., Wood, E. F., and Sheffield, J.: Land information system: An interoperable framework for high resolution land surface modeling, Environ. Model. Softw., 21, 1402–1415, doi:10.1016/j.envsoft.2005.07.004, 2006.

Kumar, S. V., Reichle, R. H., Koster, R. D., Crow, W. T., and Peters-Lidard, C. D.: Role of subsurface physics in the assimilation of surface soil moisture observations, J. Hydrometeorol., 10, 1534–1547, doi:10.1175/2009JHM1134.1, 2009.

Lapina, K., Henze, D. K., Milford, J. B., Huang, M., Lin, M., Fiore, A. M., Carmichael, G., Pfister, G. G., and Bowman, K.: Assessment of source contributions to seasonal vegetative exposure to ozone in the U.S., J. Geophys. Res. Atmos., 119, 324–340, doi:10.1002/2013JD020905, 2014.

Lefohn, A. S., Malley, C. S., Smith, L., Wells, B., Hazucha, M., Simon, H., Naik, V., Mills, G., Schultz, M. G., Paoletti, E., De Marco, A., Xu, X., Zhang, L., Wang, T., Neufeld, H. S., Musselman, R. C., Tarasick, D., Brauer, M., Feng, Z., Tang, H., Kobayashi, K., Sicard, P., Solberg, S. and Gerosa, G.: Elem. Sci. Anth., 6, 28, doi:10.1525/elementa.279, 2018.

890 Li, Q., Jacob, D. J., Park, R., Wang, Y., Heald, C. L., Hudman, R., Yantosca, R. M., Martin, R. V., and Evans, M.: North American pollution outflow and the trapping of convectively lifted pollution by upper-level anticyclone, J. Geophys. Res., 110, D10301, doi:10.1029/2004JD005039, 2005.

Lin, M., Fiore, A. M., Cooper, O. R., Horowitz, L. W., Langford, A. O., Levy II, H., Johnson, B. J., Naik, V., Oltmans, S. J.,
895 and Senff, C. J.: Springtime high surface ozone events over the western United States: Quantifying the role of stratospheric intrusions, J. Geophys. Res., 117, D00V22, doi:10.1029/2012JD018151, 2012.

Lin, M., Horowitz, L. W., Payton, R., Fiore, A. M., and Tonnesen, G.: US surface ozone trends and extremes from 1980 to 2014: quantifying the roles of rising Asian emissions, domestic controls, wildfires, and climate, Atmos. Chem. Phys., 17,
900 2943–2970, doi:10.5194/acp-17-2943-2017, 2017.

Lin, Y. and Mitchell, K. E.: The NCEP stage II/IV hourly precipitation analyses: development and applications, 19th Conf. Hydrology, San Diego, CA, available at: https://ams.confex.com/ams/pdfpapers/83847.pdf (last access: March 2020), 2005.

905 Lu, Y. Q., Harding, K., and Kueppers, L.: Irrigation Effects on Land-Atmosphere Coupling Strength in the United States, J. Clim., 30, 3671–3685, doi:10.1175/JCLI-D-15-0706.1, 2017.

Mahfouf, J.-F.: Assimilation of satellite-derived soil moisture from ASCAT in a limited-area NWP model, Q. J. R. Meteorol. Soc., 136, 784–798, doi:10.1002/qj.602, 2010.
910
Miller, D. A. and White, R. A.: A conterminous United States multilayer soil characteristics dataset for regional climate and hydrology modeling, Earth Interact., 2, 1–26, doi:10.1175/1087-3562(1998)002%3C0001:ACUSMS%3E2.3.CO;2, 1998.

Mills, G., Sharps, K., Simpson, D, Pleijel, H., Frei, M., Burkey, K., Emberson, L., Uddling, J., Broberg, M., Feng, Z.,
915 Kobayashi, K., and Agrawal, M.: Closing the global ozone yield gap: Quantification and cobenefits for multistress tolerance, Glob. Change Biol., 24, 4869–4893, doi:10.1111/gcb.14381, 2018a.

Mills, G., Sharps, K., Simpson, D., Pleijel, H., Broberg, M., Uddling, J., Jaramillo, F., Davies, W.J., Dentener, F., van den Berg, M., Agrawal, M., Agrawal, S.B., Ainsworth, E.A., Buker, P., Emberson, L., Feng, Z., Harmens, H., Hayes, F.,

920   Kopbayashi, K., Paoletti, E., and Van Dingenen, R.: Ozone pollution will compromise efforts to increase global wheat production, Glob. Change Biol., 24, 3560–3574, doi: 10.1111/gcb.14157, 2018b.

Miralles, D. G., van den Berg, M. J., Teuling, A. J., and de Jeu, R. A. M.: Soil moisture-temperature coupling: A multiscale observational analysis, Geophys. Res. Lett., 39, L21707, doi:10.1029/2012GL053703, 2012.

925

Monks, P. S., Archibald, A. T., Colette, A., Cooper, O., Coyle, M., Derwent, R., Fowler, D., Granier, C., Law, K. S., Mills, G. E., Stevenson, D. S., Tarasova, O., Thouret, V., von Schneidemesser, E., Sommariva, R., Wild, O., and Williams, M. L.: Tropospheric ozone and its precursors from the urban to the global scale from air quality to short-lived climate forcer, Atmos. Chem. Phys., 15, 8889–8973, doi:10.5194/acp-15-8889-2015, 2015.

930

Morrison, H., Thompson, G., and Tatarskii, V.: Impact of Cloud Microphysics on the Development of Trailing Stratiform Precipitation in a Simulated Squall Line: Comparison of One-and Two-Moment Schemes, Mon. Wea. Rev., 137, 991–1007, doi:10.1175/2008MWR2556.1, 2009.

935   Murray, L. T.: Lightning NO_x and Impacts on Air Quality, Curr. Pollution Rep., 2, 115–133, doi:10.1007/s40726-016-0031-7, 2016.

Nakanishi, M. and Niino, H.: Development of an improved turbulence closure model for the atmospheric boundary layer, J. Meteor. Soc. Japan, 87, 895–912, doi:10.2151/jmsj.87.895, 2009.

940

Nelson, B. R., Prat, O. P., Seo, D. J., and Habib, E.: Assessment and implications of NCEP Stage IV quantitative precipitation estimates for product intercomparisons, Weather Forecast., 31, 371–394, doi:10.1175/Waf-D-14-00112.1, 2016.

945   Oikawa, P. Y., Ge, C., Wang, J., Eberwein, J. R., Liang, L. L., Allsman, L. A., Grantz, D. A., and Jenerette, G. D.: Unusually high soil nitrogen oxide emissions influence air quality in a high-temperature agricultural region, Nat. Commun., 6, 8573, doi:10.1038/ncomms9753, 2015.

Ott, L. E., Pickering, K. E., Stenchikov, G. L., Allen, D. J., DeCaria, A. J., Ridley, B., Lin, R.-F., Lang, S., and Tao, W.-K.:
950   Production of lightning NO_x and its vertical distribution calculated from three-dimensional cloud-scale chemical transport model simulations, J. Geophys. Res., 115, D04301, doi:10.1029/2009JD011880, 2010.

Ott, L. E., Duncan, B. N., Thompson, A. M., Diskin, G., Fasnacht, Z., Langford, A. O., Lin, M., Molod, A. M., Nielsen, J. E., Pusede, S. E., Wargan, K., Weinheimer, A. J., and Yoshida, Y.: Frequency and impact of summertime stratospheric

955   intrusions over Maryland during DISCOVER-AQ (2011): New evidence from NASA's GEOS-5 simulations, J. Geophys. Res. Atmos., 121, 3687–3706, doi:10.1002/2015JD024052, 2016.

Ozdogan, M. and Gutman, G.: A new methodology to map irrigated areas using multi-temporal MODIS and ancillary data: an application example in the continental US, Remote Sens. Environ., 112, 3520–3537, doi:10.1016/j.rse.2008.04.010, 2008.

960

Pan, M., Cai, X., Chaney, N. W., Entekhabi, D., and Wood, E. F.: An initial assessment of SMAP soil moisture retrievals using high-resolution model simulations and in situ observations, Geophys. Res. Lett., 43, 9662–9668, doi:10.1002/2016GL069964, 2016.

965   Park, R. J., Hong, S. K., Kwon, H.-A., Kim, S., Guenther, A., Woo, J.-H., and Loughner, C. P.: An evaluation of ozone dry deposition simulations in East Asia, Atmos. Chem. Phys., 14, 7929–7940, doi:10.5194/acp-14-7929-2014, 2014.

Pollack, I. B., Homeyer, C. R., Ryerson, T. B., Aikin, K. C., Peichl, J., Apel, E. C., Campos, T., Flocke, F., Hornbrook, R. S., Knapp, D. J., Montzka, D. D., Weinheimer, A. J., Riemer, D., Diskin, G., Sachse, G., Mikoviny, T., Wisthaler, A., Bruning,

970   E., MacGorman, D., Cummings, K. A., Pickering, K. E., Huntrieser, H., Lichtenstern, M., Schlager, H., and Barth, M. C.: Airborne quantification of upper tropospheric NO_x production from lightning in deep convective storms over the United States Great Plains, J. Geophys. Res. Atmos., 121, 2002–2028, doi:10.1002/2015JD023941, 2016.

Rap, A., Richards, N. A. D., Forster, P. M., Monks, S. A., Arnold, S. R., and Chipperfield, M. P.: Satellite constraint on the

975   tropospheric ozone radiative effect, Geophys. Res. Lett., 42, 5074–5081, doi:10.1002/2015GL064037, 2015.

Rodell, M., Houset, P. R., Berg, A. A., and Famiglietti, J. S.: Evaluation of 10 Methods for Initializing a Land Surface Model, J. Hydrometeorol., 6, 146–155, doi:10.1175/JHM414.1, 2005.

980   Romps, D. M., Seeley, J. T., Vollaro, D. and Molinari, J.: Projected increase in lightning strikes in the United States due to global warming, Science, 346, 851–854, doi:10.1126/science.1259100, 2014.

Royer, A. and Poirier, S.: Surface temperature spatial and temporal variations in North America from homogenized satellite SMMR-SSM/I microwave measurements and reanalysis for 1979–2008, J. Geophys. Res., 115, D08110, doi:2009JD012760,

985   2010.

Sadiq, M., Tai, A. P. K., Lombardozzi, D., and Val Martin, M.: Effects of ozone–vegetation coupling on surface ozone air quality via biogeochemical and meteorological feedbacks, Atmos. Chem. Phys., 17, 3055–3066, doi:10.5194/acp-17-3055-2017, 2017.

990

Santanello, J. A., Kumar, S. V., Peters-Lidard, C. D., and Lawston, P. M.: Impact of Soil Moisture Assimilation on Land Surface Model Spinup and Coupled Land-Atmosphere Prediction, J. Hydrometeorol., 17, 517–540, doi:10.1175/jhm-d-15-0072.1, 2016.

995   Schmidt, A., Hanson, C., Chan, W. S., and Law, B. E.: Empirical assessment of uncertainties of meteorological parameters and turbulent fluxes in the AmeriFlux network, J. Geophys. Res., 117, G04014, doi:10.1029/2012JG002100, 2012.

Schneider, L., Barthlott, C., Hoose, C., and Barrett, A. I.: Relative impact of aerosol, soil moisture, and orography perturbations on deep convection, Atmos. Chem. Phys., 19, 12343–12359, doi:10.5194/acp-19-12343-2019, 2019.

1000

Seneviratne, S. I., Corti, T., Davin, E. L., Hirschi, M., Jaeger, E. B., Lehner, I., Orlowsky, B., and Teuling, A. J.: Investigating soil moisture–climate interactions in a changing climate: A review, Earth-Sci. Rev., 99, 125–161, doi:10.1016/j.earscirev.2010.02.004, 2010.

1005   Shen, L., Mickley, L. J., and Tai, A. P. K.: Influence of synoptic patterns on surface ozone variability over the eastern United States from 1980 to 2012, Atmos. Chem. Phys., 15, 10925–10938, doi:10.5194/acp-15-10925-2015, 2015.

Shindell, D., Kuylenstierna, J. C. I., Vignati, E., van Dingenen, R., Amann, M., Klimont, Z., Anenberg, S. C., Muller, N., JanssensMaenhout, G., Raes, F., Schwartz, J., Faluvegi, G., Pozzoli, L., Kupiainen, K., Höglund-Isaksson, L., Emberson, L.,
1010   Streets, D., Ramanathan, V., Hicks, K., Oanh, N. T. K., Milly, G., Williams, M., Demkine, V., and Fowler, D.: Simultaneously Mitigating Near-Term Climate Change and Improving Human Health and Food Security, Science, 335, 183–189, 2012.

Shindell, D. T., Lamarque, J.-F., Schulz, M., Flanner, M., Jiao, C., Chin, M., Young, P. J., Lee, Y. H., Rotstayn, L.,
1015   Mahowald, N., Milly, G., Faluvegi, G., Balkanski, Y., Collins, W. J., Conley, A. J., Dalsoren, S., Easter, R., Ghan, S., Horowitz, L., Liu, X., Myhre, G., Nagashima, T., Naik, V., Rumbold, S. T., Skeie, R., Sudo, K., Szopa, S., Takemura, T., Voulgarakis, A., Yoon, J.-H., and Lo, F.: Radiative forcing in the ACCMIP historical and future climate simulations, Atmos. Chem. Phys., 13, 2939–2974, doi:10.5194/acp-13-2939-2013, 2013.

1020   Solomon, S., Rosenlof, K. H., Portmann, R. W., Daniel, J. S., Davis, S. M., Sanford, T. J., and Plattner, G. K.: Contributions of stratospheric water vapor to decadal changes in the rate of global warming, Science, 327, 1219–1223, doi:10.1126/science.1182488, 2010.

Stevenson, D. S., Dentener, F. J., Schultz, M. G., Ellingsen, K., van Noije, T. P. C., Wild, O., Zeng, G., Amann, M.,
1025   Atherton, C. S., Bell, N., Bergmann, D. J., Bey, I., Butler, T., Cofala, J., Collins, W. J., Derwent, R. G., Doherty, R. M., Drevet, J., Eskes, H. J., Fiore, A. M., Gauss, M., Hauglustaine, D. A., Horowitz, L. W., Isaksen, I. S. A., Krol, M. C., Lamarque, J.-F., Lawrence, M. G., Montanaro, V., Müller, J.-F., Pitari, G., Prather, M. J., Pyle, J. A., Rast, S., Rodriguez, J. M., Sanderson, M. G., Savage, N. H., Shindell, D. T., Strahan, S. E., Sudo, K., and Szopa, S.: Multimodel ensemble simulations of present-day and near-future tropospheric ozone, J. Geophys. Res., 111, D08301, doi:10.1029/2005JD006338,
1030   2006.

Stevenson, D. S., Young, P. J., Naik, V., Lamarque, J.-F., Shindell, D. T., Voulgarakis, A., Skeie, R. B., Dalsoren, S. B., Myhre, G., Berntsen, T. K., Folberth, G. A., Rumbold, S. T., Collins, W. J., MacKenzie, I. A., Doherty, R. M., Zeng, G., van Noije, T. P. C., Strunk, A., Bergmann, D., Cameron-Smith, P., Plummer, D. A., Strode, S. A., Horowitz, L., Lee, Y. H.,
1035   Szopa, S., Sudo, K., Nagashima, T., Josse, B., Cionni, I., Righi, M., Eyring, V., Conley, A., Bowman, K. W., Wild, O., and Archibald, A.: Tropospheric ozone changes, radiative forcing and attribution to emissions in the Atmospheric Chemistry and Climate Model Intercomparison Project (ACCMIP), Atmos. Chem. Phys., 13, 3063–3085, doi:10.5194/acp-13-3063-2013, 2013.

1040   Tan, J., Petersen, W. A., and Tokay, A.: A Novel Approach to Identify Sources of Errors in IMERG for GPM Ground Validation, J. Hydrometeorol., 17, 2477–2491, doi:10.1175/JHM-D-16-0079.1, 2016.

Task Force on Hemispheric Transport of Air Pollution (HTAP): 2010 Final Assessment report, Part A: Ozone and particulate matter,   available   at:
1045   http://www.htap.org/publications/2010_report/2010_Final_Report/HTAP%202010%20Part%20A%20110407.pdf   (last access: March 2020), 2010.

Taylor, C. M., de Jeu, R. A. M., Guichard, F., Harris, P. P., and Dorigo, W. A.: Afternoon rain more likely over drier soils, Nature, 489, 423–426, doi:10.1038/nature11377, 2012.
1050
Taylor, C. M., Birch, C. E., Parker, D. J., Dixon, N., Guichard, F., Nikulin, G., and Lister, G. M. S.: Modeling soil moisture-precipitation feedback in the Sahel: Importance of spatial scale versus convective parameterization, Geophys. Res. Lett., 40, 6213–6218, doi:10.1002/2013GL058511, 2013.

1055   Toon, O. B., Maring, H., Dibb, J., Ferrare, R., Jacob, D. J., Jensen, E. J., Luo, Z. J., Mace, G. G., Pan, L. L., Pfister, L., Rosenlof, K. H., Redemann, J., Reid, J. S., Singh, H. B., Thompson, A. M., Yokelson, R., Minnis, P., Chen, G., Jucks, K. W., and Pszenny, A.: Planning, implementation, and scientific goals of the Studies of Emissions and Atmospheric Composition, Clouds and Climate Coupling by Regional Surveys (SEAC^{4}RS) field mission, J. Geophys. Res. Atmos., 121, 4967–5009, doi:10.1002/2015JD024297, 2016.

1060

Travis, K. R., Jacob, D. J., Fisher, J. A., Kim, P. S., Marais, E. A., Zhu, L., Yu, K., Miller, C. C., Yantosca, R. M., Sulprizio, M. P., Thompson, A. M., Wennberg, P. O., Crounse, J. D., St. Clair, J. M., Cohen, R. C., Laughner, J. L., Dibb, J. E., Hall, S. R., Ullmann, K., Wolfe, G. M., Pollack, I. B., Peischl, J., Neuman, J. A., and Zhou, X.: Why do models overestimate surface ozone in the Southeast United States?, Atmos. Chem. Phys., 16, 13561– 13577, doi:10.5194/acp-16-13561-2016, 2016.

1065

Tuttle, S. and Salvucci, G.: Empirical evidence of contrasting soil moisture–precipitation feedbacks across the United States, Science, 352, 825–828, doi: 10.1126/science.aaa7185, 2016.

US Federal Register: National Ambient Air Quality Standards for Ozone, 40 CFR Part 50, 51, 52, 53, and 58, 65291–65468, 1070   2015.

Val Martin, M., Heald, C. L. and Arnold, S. R.: Coupling dry deposition to vegetation phenology in the Community Earth System Model: Implications for the simulation of surface O_3, Geophys. Res. Lett., 41, 2988–2996, doi:10.1002/2014GL059651, 2014.

1075

Wang, Y., Ma, Y.-F., Eskes, H., Inness, A., Flemming, J., and Brasseur, G. P.: Evaluation of the CAMS global atmospheric trace gas reanalysis 2003–2016 using aircraft campaign observations, Atmos. Chem. Phys., 20, 4493–4521, doi:10.5194/acp-20-4493-2020, 2020.

1080   Wang, Z., Zeng, X., and Decker, M.: Improving snow processes in the Noah land model, J. Geophys. Res., 115, D20108, doi:10.1029/2009JD013761, 2010.

Wesely, M. L.: Parameterization of surface resistances to gaseous dry deposition in regional-scale numerical models, Atmos. Environ., 41, 52–63, doi:10.1016/j.atmosenv.2007.10.058, 1989.

1085

Wong, A. Y. H., Geddes, J. A., Tai, A. P. K., and Silva, S. J.: Importance of dry deposition parameterization choice in global simulations of surface ozone, Atmos. Chem. Phys., 19, 14365–14385, doi:10.5194/acp-19-14365-2019, 2019.

Wong, J., Barth, M. C., and Noone, D.: Evaluating a lightning parameterization based on cloud-top height for mesoscale

1090   numerical model simulations, Geosci. Model Dev., 6, 429–443, doi:10.5194/gmd-6-429-2013, 2013.

World Health Organization: Review of evidence on health aspects of air pollution–REVIHAAP Project, available at:
http://www.euro.who.int/__data/assets/pdf_file/0004/193108/REVIHAAP-Final-technical-report-final-version.pdf?ua=1
(last access: March 2020), 2013.

1095

Wu, Z., Schwede, D. B., Vet, R., Walker, J. T., Shaw, M., Staebler, R., and Zhang, L.: Evaluation and intercomparison of
five North American dry deposition algorithms at a mixed forest site, J. Adv. Model. Earth Syst., 10, 1571–1586,
doi:10.1029/2017MS001231, 2018.

1100   Yin, J. and Zhan, X: Impact of bias-correction methods on effectiveness of assimilating SMAP soil moisture data into NCEP
global forecast system using the ensemble Kalman filter, IEEE Geosci. Remote Sens. Lett., 15, 659–663,
doi:10.1109/LGRS.2018.2806092, 2018.

Zaussinger, F., Dorigo, W., Gruber, A., Tarpanelli, A., Filippucci, P., and Brocca, L.: Estimating irrigation water use over

1105   the contiguous United States by combining satellite and reanalysis soil moisture data, Hydrol. Earth Syst. Sci., 23, 897–923,
doi:10.5194/hess-23-897-2019, 2019.

Zaveri, R. A. and Peters, L. K.: A new lumped structure photochemical mechanism for large-scale applications, J. Geophys.
Res., 104, 30387–30415, doi:10.1029/1999JD900876, 1999.

1110

Zaveri, R. A., Easter, R. C., Fast, J. D., and Peters, L. K.: Model for simulating aerosol interactions and chemistry
(MOSAIC). J. Geophys. Res., 113, D13204, doi:10.1029/2007JD008782, 2008.

Zhang, L., Jacob, D. J., Boersma, K. F., Jaffe, D. A., Olson, J. R., Bowman, K. W., Worden, J. R., Thompson, A. M., Avery,

1115   M. A., Cohen, R. C., Dibb, J. E., Flock, F. M., Fuelberg, H. E., Huey, L. G., McMillan, W. W., Singh, H. B., and
Weinheimer, A. J.: Transpacific transport of ozone pollution and the effect of recent Asian emission increases on air quality
in North America: an integrated analysis using satellite, aircraft, ozonesonde, and surface observations, Atmos. Chem. Phys.,
8, 6117–6136, doi:10.5194/acp-8-6117-2008, 2008.

1120   Zhang, L., Lin, M., Langford, A. O., Horowitz, L. W., Senff, C. J., Klovenski, E., Wang, Y., Alvarez II, R. J.,
Petropavlovskikh, I., Cullis, P., Sterling, C. W., Peischl, J., Ryerson, T. B., Brown, S. S., Decker, Z. C. J., Kirgis, G., and

Conley, S.: Characterizing sources of high surface ozone events in the southwestern U.S. with intensive field measurements and two global models, Atmos. Chem. Phys. Discuss., doi:10.5194/acp-2019-990, in press, 2019.

1125   Zhao, M., Golaz, J.-C., Held, I. M., Guo, H., Balaji, V., Benson, R., Chen, J.-H., Chen, X., Donner, L. J., Dunne, J. P., Dunne, K., Durachta, J., Fan, S.-M., Freidenreich, S. M., Garner, S. T., Ginoux, P., Harris, L. M., Horowitz, L. W., Krasting, J. P., Langenhorst, A. R., Liang, Z., Lin, P., Lin, S.-J., Malyshev, S. L., Mason, E., Milly, P. C. D., Ming, Y., Naik, V., Paulot, F., Paynter, D., Phillipps, P., Radhakrishnan, A., Ramaswamy, V., Robinson, T., Schwarzkopf, D., Seman, C. J., Shevliakova, E., Shen, Z., Shin, H., Silvers, L. G., Wilson, J. R., Winton, M., Wittenberg, A. T., Wyman, B., and Xiang, B.:

1130   The GFDL Global Atmosphere and Land Model AM4.0/LM4.0: 1. Simulation Characteristics With Prescribed SSTs, J. Adv. Model. Earth Syst., 10, 691–734, doi:10.1002/2017MS001208, 2018.

Zhu, J. and Liang, X.-Z.: Impacts of the Bermuda High on regional climate and ozone over the United States, J. Clim., 26, 1018–1032, doi:10.1175/JCLI-D-12-00168.1, 2013.

Tables

Table 1: Summary of WRF-Chem simulations conducted in this study.

Case name	Horizontal/vertical resolutions	Analyzed period (field campaign)	Assimilated SM data (version; resolution)	Anthropogenic emission inputs for various chemical species
Base	12 km/63 layer	16-28 August 2016 (ACT-America)	none	NEI 2016 beta
Assim			SMAP enhanced passive (version 2; 9 km)	NEI 2016 beta
NEI14			none	NEI 2014
SEACf	25 km/27 layer	12-24 August 2013 (SEAC^{4}RS)	none	NEI 2014
SEACa			ESA CCI passive (version 04.5; 0.25°)	NEI 2014

Acronyms: ACT: Atmospheric Carbon Transport; ESA CCI: European Space Agency Climate Change Initiative; NEI: National Emission Inventory; SEAC^{4}RS: Studies of Emissions and Atmospheric Composition, Clouds and Climate Coupling by Regional Surveys; SM: Soil Moisture; SMAP: Soil Moisture Active Passive; WRF-Chem: Weather Research and Forecasting model with online Chemistry

Table 2: The number of model grids with surface MDA8 O$_3$ exceedance false alarms (i.e., WRF-Chem MDA8 O$_3$>70 ppbv but the observed MDA8 O$_3$<=70 ppbv) from the 12 km WRF-Chem simulations. Degradations and improvements from the base case are highlighted in red and green, respectively.

Days of August 2016	Referring to AQS observations			Referring to CASTNET observations		
	Base	Assim	NEI14	Base	Assim	NEI14
16	0	0	0	0	0	0
17	0	0	0	0	0	0
18	1	3	4	0	0	0
19	9	9	10	0	0	0
20	4	4	13	0	0	1
21	0	0	0	0	0	0
22	0	0	0	0	0	0
23	1	1	1	0	0	0
24	1	1	2	0	0	0
25	1	1	2	0	0	0
26	6	5	9	1	0	1
27	0	0	0	0	0	0
28	6	6	14	0	0	0

Figures
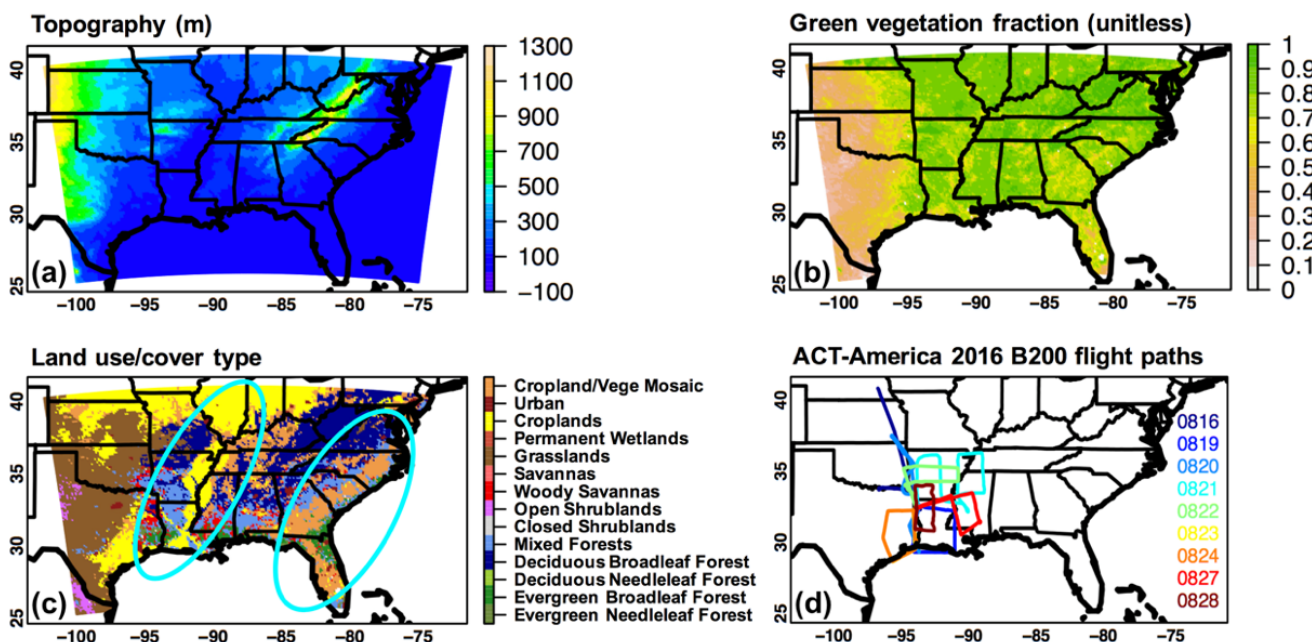
Figure 1: (a) Terrain heights; (b) August 2016 green vegetation fraction; and (c) grid-dominant land use/cover categories used in the 12 km LIS/WRF-Chem simulations. (d) B-200 flight paths in the southeastern US during the 2016 ACT-America campaign. Cyan-blue circles in (c) denote the approximate locations of areas with high irrigation water use based on literature. Similar model domains, consistent sources of geographical inputs and meteorological forcings were used in 12 km and 25 km LIS/WRF-Chem simulations.
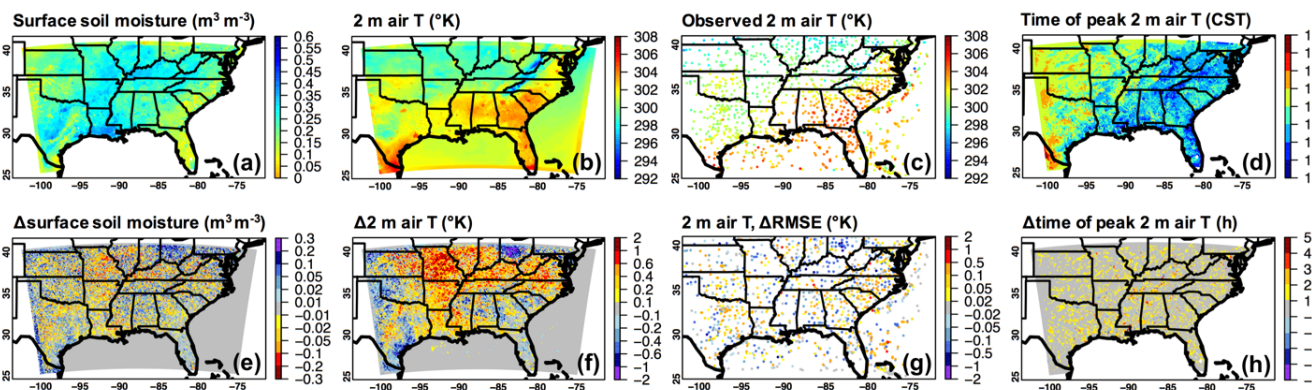
Figure 2: Period-mean (16-28 August 2016) WRF-Chem base case (a) surface soil moisture at initial times; (b) daytime 2 m air temperature (T); and (d) time of daily peak air T in US Central Standard Time (CST), as well as (e;f;h) the impacts of SMAP DA on these fields. Observed daytime 2 m air T and the impact of the SMAP DA on RMSEs of the daytime 2 m air T are shown in (c) and (g), respectively.
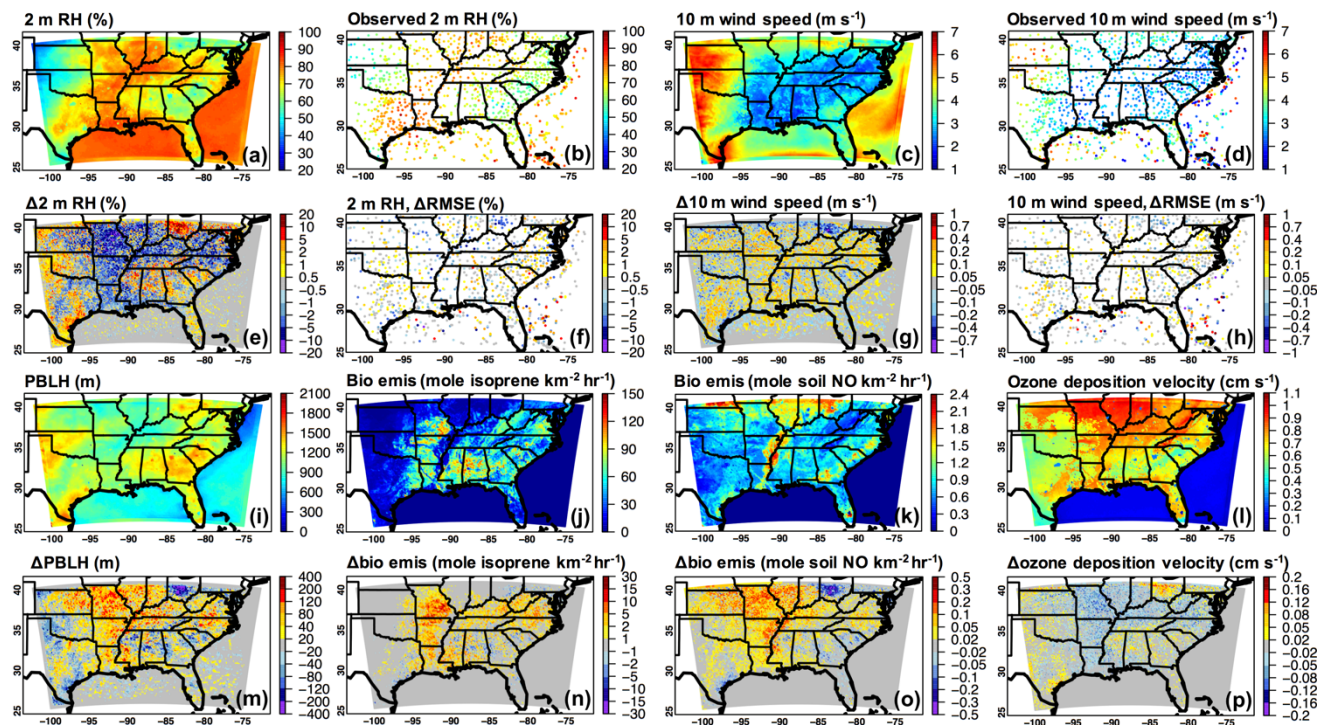
Figure 3: Period-mean (16-28 August 2016) WRF-Chem base case daytime (a) 2 m relative humidity (RH); (c) 10 m wind speed; (i) PBLH; biogenic emissions of (j) isoprene and (k) soil NO; and (l) O$_3$ deposition velocity, as well as (e;g;m;n;o;p) the impacts of SMAP DA on these model fields. Observed daytime 2 m RH and surface wind speed, as well as the impacts of the SMAP DA on RMSEs of these fields are shown in (b;f) and (d;h), respectively. Additional biogenic emissions and deposition results are shown in Figure S4.
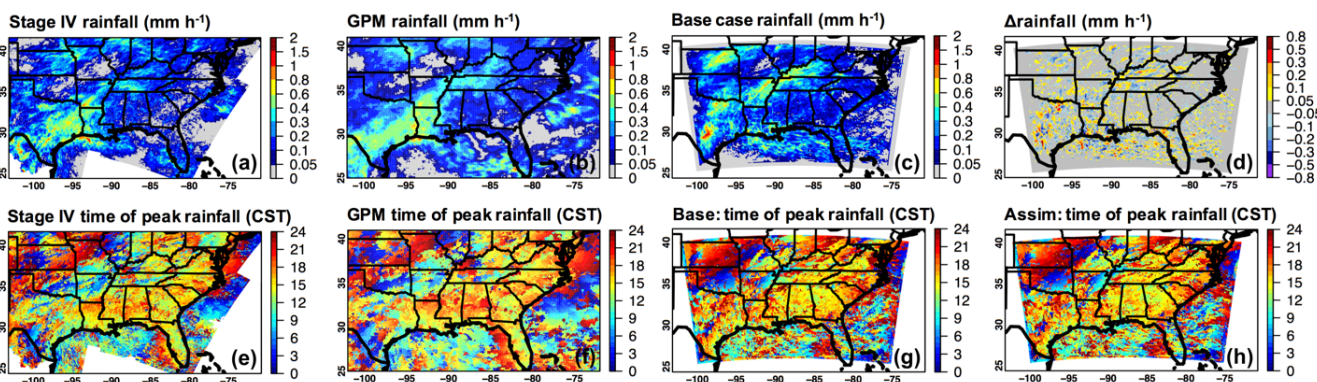
Figure 4: Period-mean (16-28 August 2016) (a-d) rainfall rate and (e-h) time of peak rainfall in US Central Standard Time (CST) from (a;e) the national Stage IV Quantitative Precipitation Estimates product; (b;f) the Global Precipitation Measurement; and (c;g) WRF-Chem base case. Results from the WRF-Chem "assim" case are indicated in (d;h).
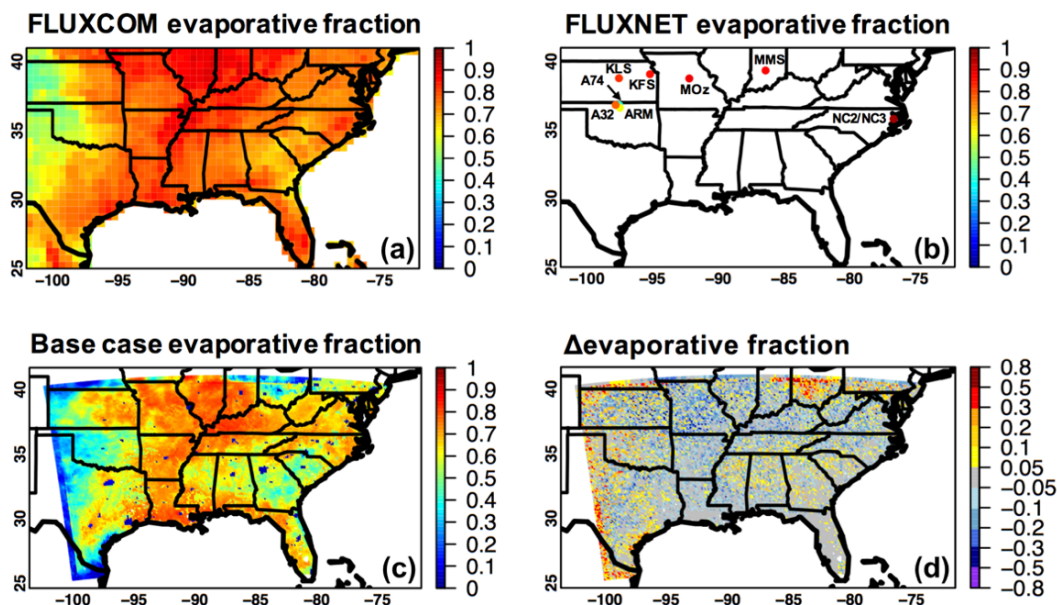
Figure 5: Period-mean (16-28 August 2016) daily evaporative fraction, defined as: daily latent heat/(daily latent heat+daily sensible heat), from (a) a FLUXCOM product; (b) selected FLUXNET sites; and (c) WRF-Chem base case. (d) shows the impact of the SMAP DA on WRF-Chem EF. Additional evaluation results for latent and sensible heat fluxes at the focused FLUXNET sites are presented in Figure S3.
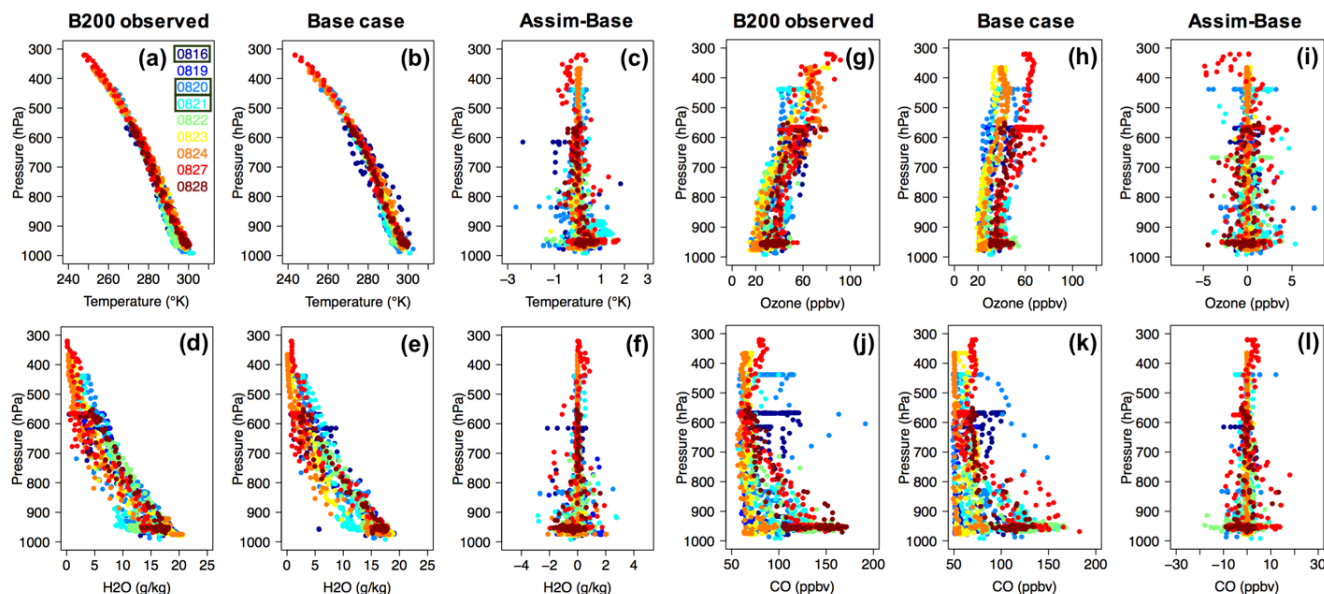
Figure 6: Vertical profiles of (a) air temperature; (d) water vapor mixing ratio (H_2O); (g) O_3; and (j) carbon monoxide (CO) observed on the B-200 aircraft during the ACT-America 2016 campaign, based on a 1-minute averaged dataset. Their WRF-Chem counterparts from the base case and the impacts of the SMAP DA are shown in (b;e;h;k) and (c;f;i;l), respectively. The different colors distinguish samples taken on various flight days, and the B-200 paths on these flight days are shown in Figure 1d. Fights on 16, 20, 21 of August 2016 were conducted under stormy weather conditions as highlighted in (a), whereas the B-200 flew under fair weather conditions during other flights.
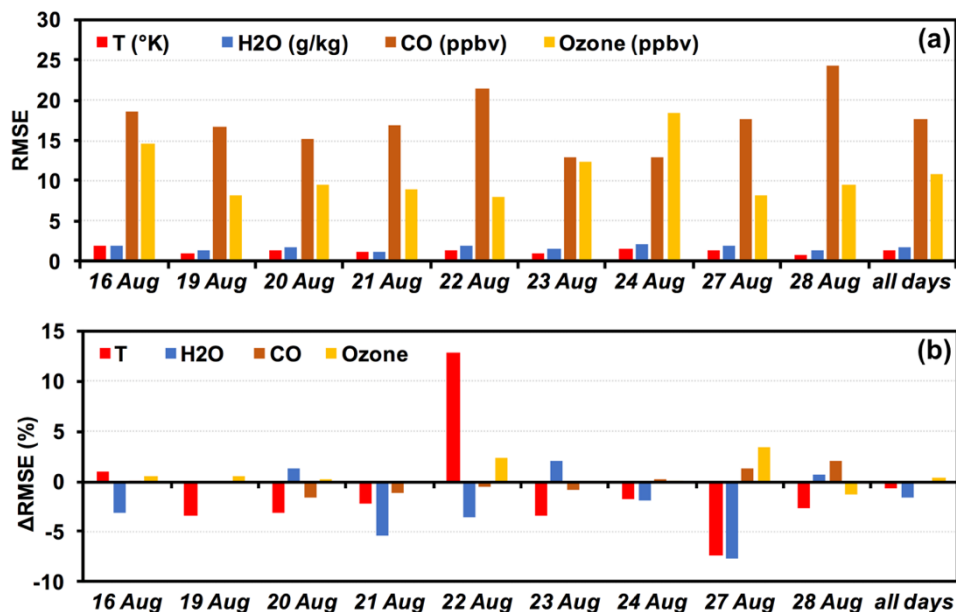
Figure 7: Evaluation of WRF-Chem results with the B-200 aircraft observations during the ACT-America 2016 campaign: (a) the RMSEs of air temperature (T), water vapor mixing ratio (H₂O), carbon monoxide (CO) and ozone of the model base case; and (b) the impacts of the SMAP DA on RMSEs of these variables. The B-200 fight paths by day are shown in Figure 1d.
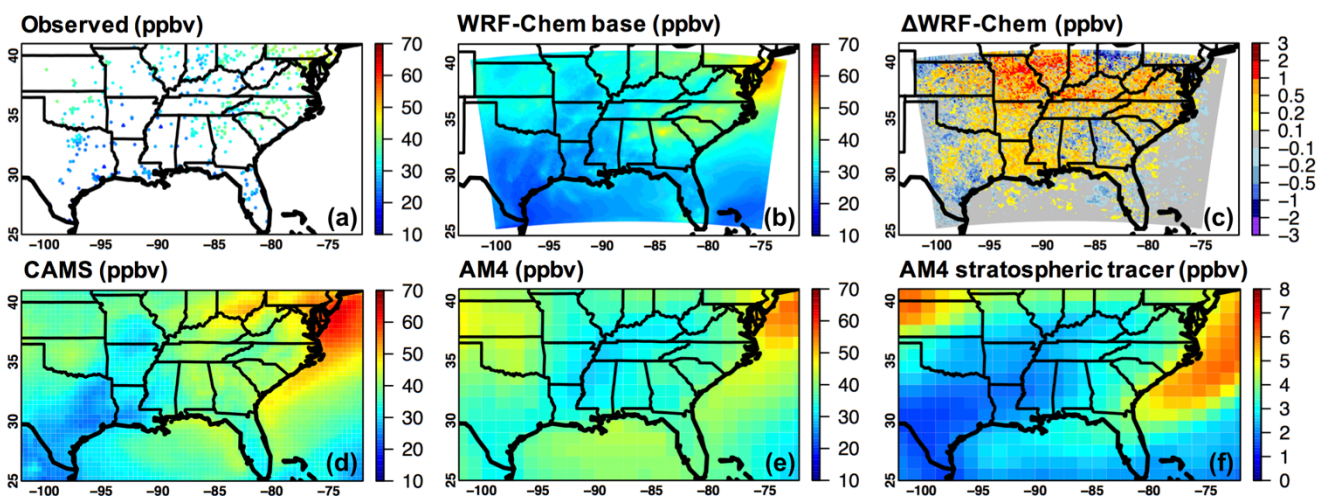
Figure 8: Period-mean (16-28 August 2016) daytime surface O₃ from (a) the EPA AQS (filled circles) and CASTNET (triangles) sites; (b) WRF-Chem base case; (d) CAMS; and (e) GFDL AM4. (c) shows the impact of the SMAP DA on WRF-Chem modeled daytime surface O₃. (f) indicates stratospheric influences on daytime surface O₃ based on the AM4 stratospheric O₃ tracer output.
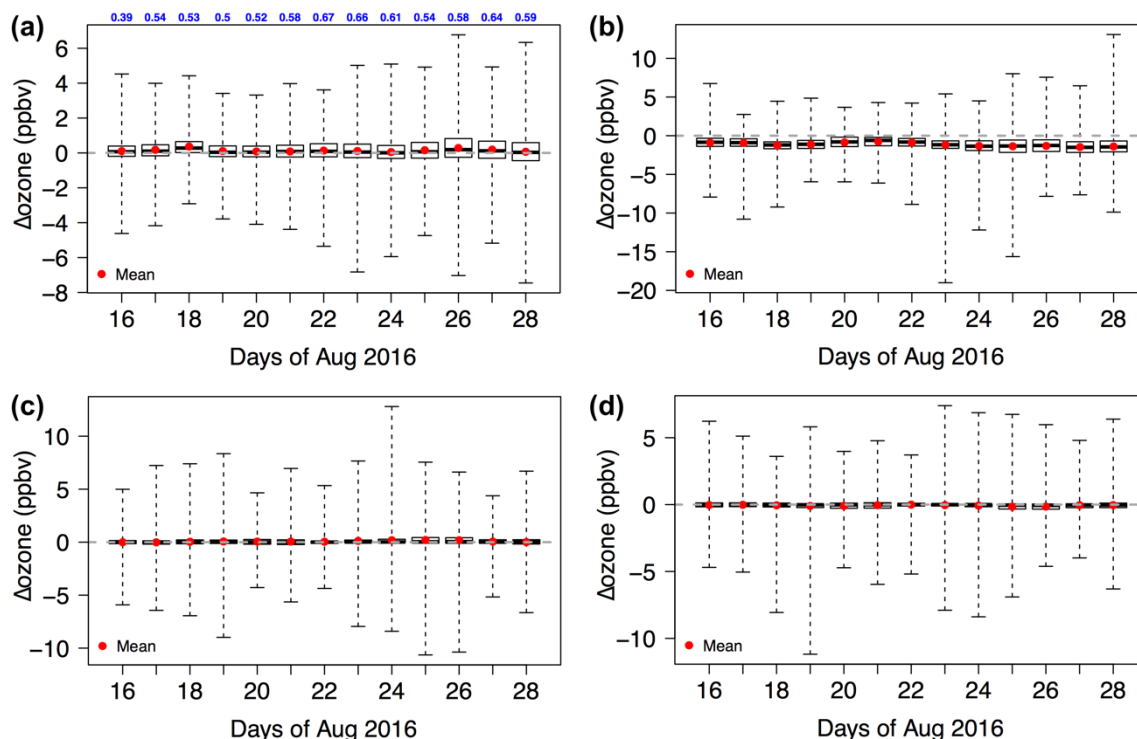
Figure 9: Box-and-whisker plots of WRF-Chem daytime O$_3$ responses to (a;c) the SMAP DA; and (b;d) updating anthropogenic emissions from NEI 2014 to NEI 2016 beta. (a-b) and (c-d) show O$_3$ changes at the surface (only for terrestrial model grids, 68% of all model grids) and at ~400 hPa (in all model grids), respectively. Blue text in (a) are spatial correlation coefficients between WRF-Chem daily daytime 2 m air temperature changes and O$_3$ changes due to the SMAP DA. Note the different Y-axis ranges.
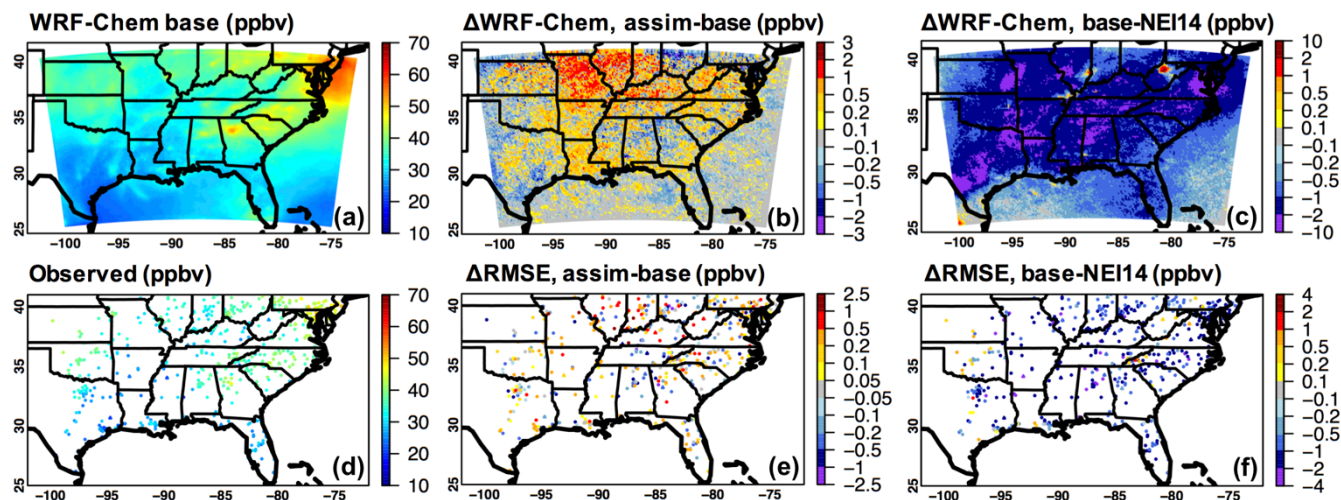
Figure 10: Period-mean (16-28 August 2016) daily maximum 8-h average (MDA8) surface O$_3$ from (a) WRF-Chem base case and (d) the EPA AQS (filled circles) and CASTNET (triangles) sites. The impact of the SMAP DA on WRF-Chem MDA8 O$_3$ and the associated RMSE changes are shown in (b) and (e), respectively. The benefit of using NEI 2016 beta instead of NEI 2014 is indicated in (c;f).
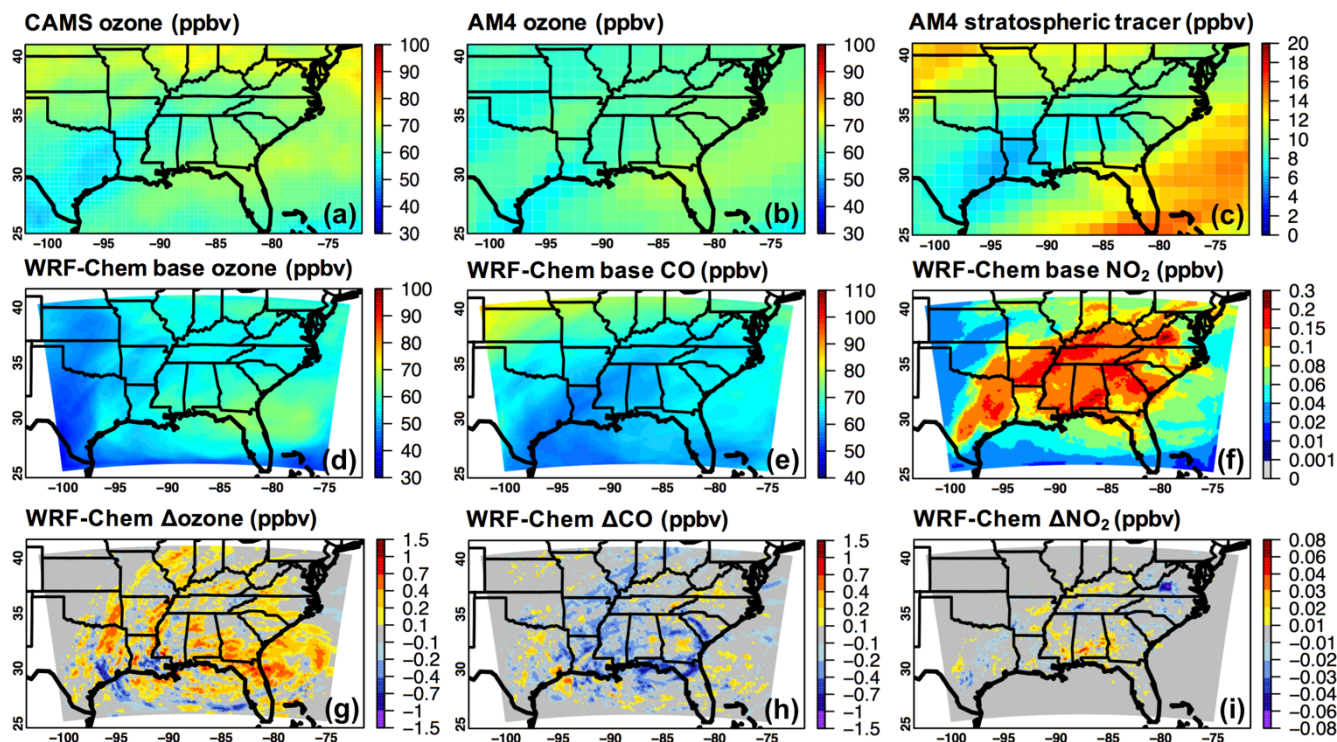
Figure 11: Period-mean (16-28 August 2016) daytime O$_3$ in the upper troposphere (i.e., the model levels close to 400 hPa) from (a) CAMS; (b) GFDL AM4; and (d) WRF-Chem base case. (g) shows the impact of the SMAP DA on WRF-Chem modeled daytime O$_3$ in the upper troposphere, and (c) indicates the stratospheric influences on O$_3$ at these altitudes based on the AM4 stratospheric O$_3$ tracer output. Period-mean daytime CO and NO$_2$ from WRF-Chem base case as well as their responses to the SMAP DA are shown in (e;h) and (f;i), respectively.

1205
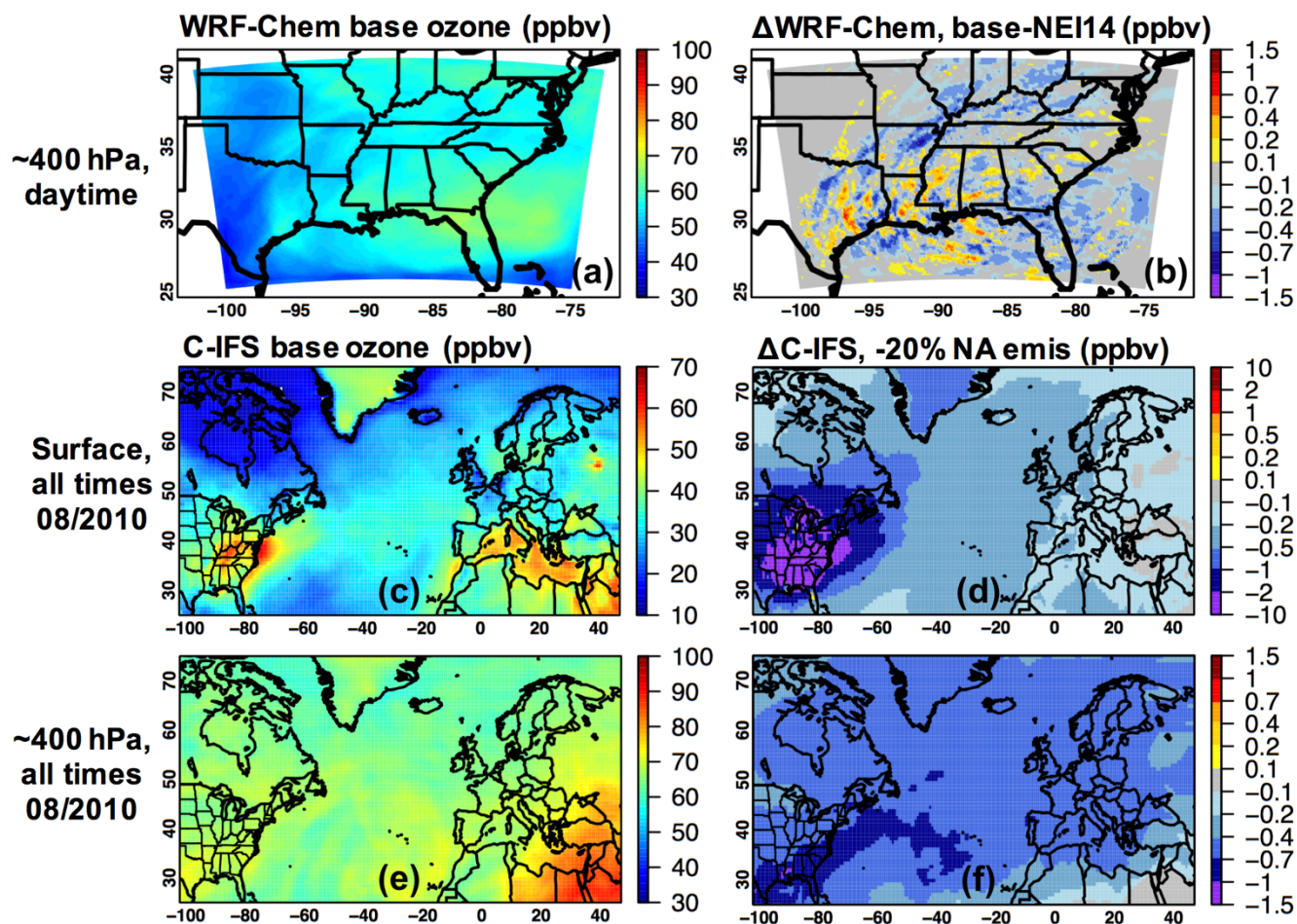
Figure 12: (a;c;e) O₃ and (b;d;f) impacts of emission changes on O₃ from: (a-b) WRF-Chem at ~400 hPa, during the daytimes of 16-28 August 2016; (c-d) the Composition-Integrated Forecasting System (C-IFS) at the surface, during all times of August 2010; and (e-f) the C-IFS at ~400 hPa, during all times of August 2010. These C-IFS simulations were performed at 0.7°×0.7° in support of the HTAP2 (Huang et al., 2017a). "NA" in (d) stands for "North American".

1210